

Testing cosmological variability of the
proton-to-electron mass ratio on the
basis of the spectrum of **Q0347-383**

Diploma Thesis

Martin Wendt

Hamburger Sternwarte
Department Physik
Universität Hamburg

19th September 2006

”We shall not cease from exploration
And the end of all our exploring
Will be to arrive where we started
And know the place for the first time.”
-T.S. Eliot, Four Quartets

Contents

1	Introduction	1
2	Background	2
2.1	Cosmology of varying fundamental physical constants	2
2.2	Quasar absorption line spectra	2
2.2.1	Observed line profiles	5
2.2.2	Equivalent width and curve of growth	9
2.3	Molecular Hydrogen H ₂	12
2.3.1	Occurrences of intergalactic H ₂	12
2.3.2	Energy levels of H ₂	13
2.4	How to measure a possible variation of μ ?	17
2.4.1	Sensitivity coefficients K_i	17
2.4.2	Distinguish cosmological redshifts from variation of μ	18
3	Methods and Data	20
3.1	Observation	20
3.1.1	The Quasar Q0347-383	20
3.2	Data reduction	21
3.2.1	Binning of observed data	21
3.2.2	Coadding spectra from different observation runs	22
3.3	Transition frequency tables for H ₂	23
3.4	Fitting data	24
3.4.1	χ^2 Fitting	24
3.4.2	Fitting procedures	24
3.4.3	Simultaneous fit vs. coadded fit	26
3.4.4	Background considerations	27
3.5	Simulations	28
4	Data analysis	30
4.1	Identification of H ₂ lines	30
4.2	Curve of growth	30
4.3	Fitting of H ₂ features	33
4.3.1	On possible shifts between the observed spectra	34
4.3.2	Simultaneous fits for all nine spectra	35
4.3.3	Profiles and fits of selected H ₂ features	38

5	Results	42
5.1	Evaluation of the data analysis	42
6	Error analysis	46
6.1	Line fits	46
6.2	Significance of detection of variation	48
6.2.1	Pearson product-moment correlation coefficient	48
6.2.2	Dependency of the result on single lines	48
6.2.3	Fit to data with errors in both coordinates	51
6.2.4	Goodness of fit	52
6.3	Conclusions	54
7	Outlook	56
	Acknowledgements	59
	References	61
	Erklärung	65

Zusammenfassung/Abstract

Die vorliegende Diplomarbeit beschäftigt sich mit der Methodik zur Bestimmung einer möglichen Variation des Proton-Elektron Massenverhältnisses anhand von Quasarspektren. Im Speziellen wird das Absorptionslinienspektrum des Quasars Q0347-383 analysiert, um einen positiven Befund von Ivanchik et al. (2005) gegebenenfalls zu verifizieren oder andernfalls mögliche Fehlerquellen zu diskutieren und zu bewerten. Q0347-383 ist ein heller Quasar 17ter Größe mit einer Rotverschiebung von $z = 3.025$, dessen Spektrum Absorptionslinien von HI-Systemen besonders hoher Säulendichte (DLA¹) aufweist. In einem dieser DLA-Systeme ist molekularer Wasserstoff H₂ nachweisbar, der sich an Staubteilchen bildet. Die Übergangsenergien zwischen verschiedenen Rotations- und Vibrationsniveaus von H₂ sind von der reduzierten Masse $\mu = \frac{m_1 \times m_2}{m_1 + m_2}$ des Moleküls abhängig. Sind diese Abhängigkeiten für jeden Übergang bekannt, ermöglicht die exakte Messung der Wellenlänge der beobachteten Absorptionslinien eine Bestimmung der reduzierten Masse bei $z = 3.025$ und somit einer möglichen Abweichung des Proton-Elektron-Massenverhältnisses vom heutigen Wert von 1836.15267261(85) (Mohr and Taylor 2005). Der zu bestimmende Parameter ist die individuelle Rotverschiebung jeder Absorptionslinie. Sie beinhaltet zunächst die kosmologische Rotverschiebung des DLA-Absorbers und einen möglichen additiven Anteil auf Grund von Übergangsenergien, die bei gegebener Variation von den lokalen Energiedifferenzen der einzelnen Niveaus abweichen. Hinzu kommt eine makroskopische Geschwindigkeitskomponente die sich nicht separat bestimmen lässt. Dazu werden die Positionen der identifizierten Absorptionslinien mit einer auf Evolutionsstrategien basierenden Fitprozedur bestimmt und auf eine Korrelation mit ihrer zugehörigen Sensitivität auf eine Änderung der reduzierten Masse hin überprüft. Eine Analyse von 39 beobachteten H₂-Absorptionslinien kann den positiven Befund einer Variation nicht mit hinreichender Signifikanz bestätigen. Eine Auswahl von 32 dieser Linien gibt keinen Hinweis auf jedwede Variation des Massenverhältnisses. Zudem gibt es Hinweise auf systematische, bislang nicht hinreichend berücksichtigte Fehlerquellen. Diese Arbeit umfasst eine detaillierte Darstellung der Analyse von Absorptionsspektren und der Methodik zur Bestimmung einer möglichen Variation des Massenverhältnisses und geht weiterhin auf mögliche Fehlerquellen und deren Auswirkungen ein.

¹Aus dem Englischen von *damped Ly α systems*.

This diploma thesis examines the methods and procedures involved in the determination of a possible variation of the proton-electron mass ratio on cosmological time scales. The method of quasar absorption line spectroscopy constitutes the basis of the approach discussed in this thesis. Q0347-383 is a bright quasar of 17th magnitude at a redshift of $z = 3.025$. Its spectrum shows absorption systems of high HI column density leading to saturated absorption features with prominent damping wings, hence referred to as *damped Ly α systems* (DLA). One of those DLA systems contains observable molecular hydrogen H₂ apparent in optically thin absorption features. The electro-vibro-rotational transitions of H₂ depend differently on the reduced mass $\mu = \frac{m_1 \times m_2}{m_1 + m_2}$ of the H₂ molecule.

Knowing the individual sensitivity for changes in the proton-to-electron mass ratio of each transition the in situ mass ratio at $z = 3.025$ can be determined from exact redshift measurements of the observed transitions. A possible deviation from the local value of 1836.15267261(85) (Mohr and Taylor 2005) can then be ascertained. The required observable parameter is solely the redshift. It contains the cosmological redshift of the DLA system and a possible additive component rising from possible changes in the individual transition frequencies due to variation in the proton-to-electron mass ratio.

The redshifts of the identified H₂ absorption features are determined by a fitting procedure driven by an evolution strategy. The obtained redshifts are tested for a correlation with their individual sensitivity towards changes in μ .

The analysis of 39 observed H₂ features cannot reproduce the significance achieved by previous works (e.g. Ivanchik et al. 2005; Reinhold et al. 2006). The analysis of a subset of 32 lines shows no detectable correlation at all. A positive variation of the proton-to-electron mass cannot be verified. A statistical analysis and several simulations indicate systematic non-negligible sources of errors.

This work includes a detailed description of the methods applied to determine a possible variation of fundamental physical constants by means of quasar absorption spectroscopy. Furthermore different systematic errors are exemplified and evaluated.

1 Introduction

The idea of varying fundamental physical constants is probably as old as the first definition of constants. Among the most prominent who formulated such ideas in the last century were Milne and Dirac in the late 1930s who considered a time-dependant gravitational constant. Later, Teller and Dyson brought up a more specified theory of a varying fine structure constant α . The famous Gamow paper (Gamow 1967) that suggested a rather strong α -variation brought about the first usage of quasar spectra for setting bounds on a possible variation rate of a fundamental physical constant. The interest in varying constants increased greatly since the 1980s due to new developments in the Kaluza-Klein and supergravity models of unifications of all physical interactions. Contemporary theories of fundamental interactions, particularly those subsumed as String-theories allow for all kinds of variations of fundamental constants in the course of the evolution of the universe. Variations of the coupling constants of strong and electroweak interactions would affect the masses of elementary particles dependant on the model for the expanding universe.

It is up to cosmology to achieve first estimates and constraints of possible variations since laboratory experiments lack the precision and spatial or temporal coverage. A recent analysis of HE 0515-4414 by Chand et al. (2006) yielded a result for the fine structure constant that is in good agreement with no variation at the current level of accuracy. A claimed detection of significant positive variation in the proton-to-electron mass-ratio Ivanchik et al. (2005) and a later refinement by Reinhold et al. (2006) to $\Delta\mu/\mu = (2.4 \pm 0.6) \times 10^{-5}$ launched numerous theories with different scenarios to interpret the new data. The subject is still under heavy debate and confirmation of the results and methods is required (see e.g. Murphy et al. 2001; Levshakov et al. 2006; Webb et al. 2003).

This diploma thesis deals with the methods of ascertaining a possible variation in the proton-to-electron mass ratio μ via analysis of quasar absorption line spectroscopy as proposed by Varshalovich and Levshakov in 1993.

During the period of this thesis a refined positive variation was reported and the main focus of this work is to evaluate and verify the methods involved in analysis of absorption spectra in general and detection of μ variation in particular. After an introduction to the theoretical background and the physics involved, the applied methods are illustrated. The proximate results are pictured briefly and analysed in further detail in the following discussion. The thesis concludes with future prospects on the subject.

2 Background

2.1 Cosmology of varying fundamental physical constants

The Kaluza-Klein theory is a generalisation of Einstein's general relativity to (originally) five dimensions by Theodor Kaluza in 1921. It contains both the Einstein equation and the Maxwell equations as special cases. Oskar Klein later proposed to imagine the new extra dimension as being curled up in a way that would keep us from noticing it. These considerations had a great impact on the whole field of string theory. Since the base space of Kaluza-Klein theory need not even be four-dimensional space-time, there is a large variety of competing models. In those Kaluza-Klein theories the fundamental constants appear as a mere manifestation of the scale-length in the extra dimensions, additional to the usual four space-time ones. An observable variation let alone a direct value is not predicted but allowed for and depending on the various models even assumed to be likely.

There is a wide range of theoretically possible connections between the fine structure constant α and the proton-electron mass ratio $\mu = m_p/m_e$. In most models variations in α lead to variations in the electron mass via the electron self-energy and in the proton mass via the electrostatic energy contained inside a proton. Yet there is neither consensus on a theory behind such variations nor on its temporal or spatial homogeneity or inhomogeneity. The more important are observational findings to give a constraint or even a first estimation of such variations. There are numerous works on a possible variation of α and the whole matter is still under debate.

It has become evident that the observational examination of a possible variation of any fundamental constant sets high demands on both the data acquisition and the methods of analysis.

2.2 Quasar absorption line spectra

Quasi-Stellar Objects, QSOs, or quasars were first identified as such by Maartin Schmidt and Allan R. Sandage in 1963/64. At the present state of knowledge Quasars correspond to active galactic nuclei (AGN) containing a central black hole as illustrated schematically in Figure 2.1. The enormous energy output placing

the QSOs among the brightest known objects arises from matter accreting and impacting a supermassive central black hole. The core region of a configuration like that easily exceeds the host galaxy in luminosity and was first identified as point sources on early photographs. Hence the name quasar, deriving from the observation of *quasi-stellar radio sources* as quasars were formerly observed only by their huge radiolobes in the radio-range. Due to their immense brightness

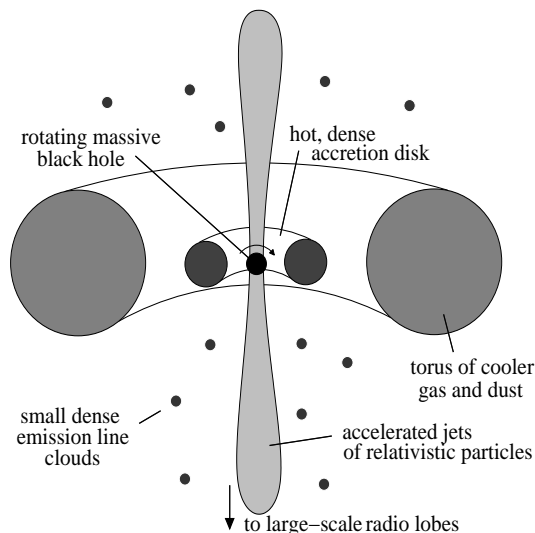


Figure 2.1: Current quasar model. The accretion disk around a central supermassive black hole at its bright centre with the intense jets of accelerated particles that form the large radio lobes observed up to 100 pc further outwards. The central region is surrounded by a cooler dust torus and numerous smaller excited gas clouds that produce further emission features in the intrusive quasar spectrum.

(up to $10^{15}L_{\odot}$), QSOs can be used as background sources against which intervening gas can be observed. The distances to individual QSOs are in the order of Gpc. Gas along the line of sight produces absorption lines and the redshift of these absorption lines z_{abs} in general reflects the cosmological distance of the absorbing system. The objects probed are not the QSOs themselves, but the intervening material $z_{\text{abs}} < z_{\text{QSO}}$. Figure 2.2 illustrates the formation of such a quasar absorption line spectrum. Absorbers at different cosmological redshifts absorb parts of the quasar spectrum according to their composition leading to low fluxes at wavelengths of the redshifted absorption lines. This illustration is simplified as the absorbing material is less grouped in distinctive clouds as in a more complex density distribution. In this example absorber B produces strong saturated absorption features corresponding to a dense region of intergalactic matter – possibly an early galaxy. Historically, absorption systems are

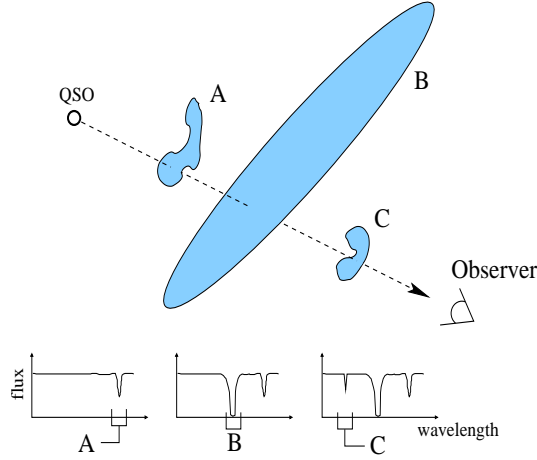


Figure 2.2: The principle of the formation of quasar absorption spectra. The light from the Quasar on its way to the observer passes through different absorbers, A-C respectively at different redshifts and with varying densities.

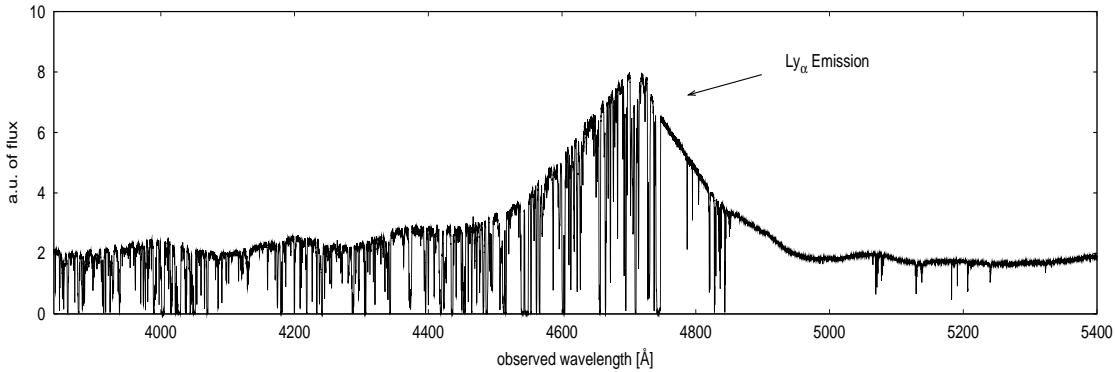


Figure 2.3: Exemplary spectrum of the quasar HE2347 at $z = 2.885$ with broad Ly α emission peak and blueward Ly α forest.

classified according to their neutral hydrogen column density $N(\text{H I})$, the number of atoms along the line of sight per unit area. Each structure along the line of sight produces an absorption feature in the quasar spectrum at a wavelength of $\lambda_{\text{obs}} = \lambda_{\text{rest}}(1 + z_{\text{abs}})$, where z_{abs} is the redshift of the absorbing gas and λ_{rest} is the restframe wavelength of the absorbing transition. $\lambda_{\text{rest}} = 1215.67 \text{ \AA}$ is the rest wavelength of the prominent Ly α transition. Its emission peak is clearly visible in the spectrum of quasar HE2347 in Figure 2.3. Observed at a wavelength of about 4715 \AA a first estimation of the quasars redshift can immediately be given as $z = 4715/1216 - 1 = 2.88$ which matches well with the ascertained redshift

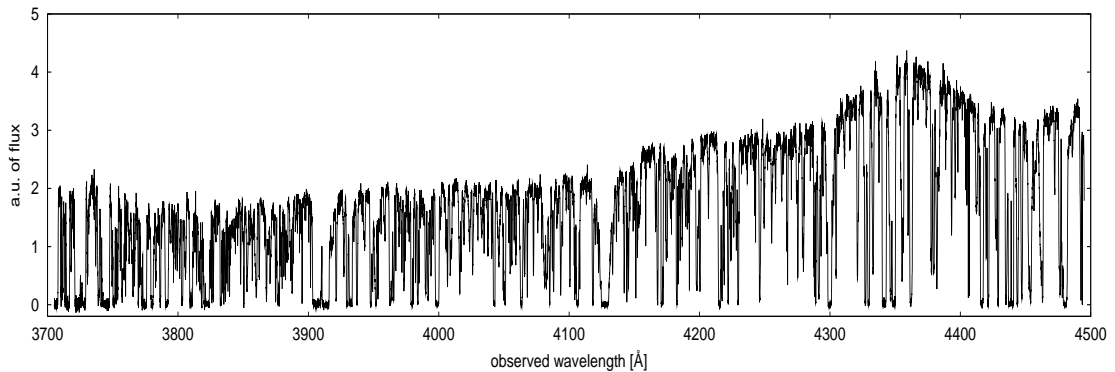


Figure 2.4: Coadded spectrum of Q0347-383 at $z = 3.22$ with strong Ly α forest characteristic for a high redshift-quasar.

of $z = 2.885$. Since $z_{\text{abs}} < z_{\text{QSO}}$, the redshift of the quasar, the Ly α absorption lines form a "forest" at wavelengths blueward of the Ly α emission. Figure 2.4 shows the quasar absorption line spectrum in the range analysed in this work. The Ly α forest is predominant. The region redward of the Ly α emission peak is populated only by absorption through other elements with transitions at larger λ_{rest} for example C II at 1393 Å. The number of systems per unit redshift decreases dramatically with increasing column density. Absorption systems with a hydrogen column density $N(\text{H I}) > 10^{20.3} \text{cm}^{-2}$ are referred to as *damped Ly α systems* (DLA). DLAs are systems with such large column densities that the damping wings of Ly α are optically thick, so that the Ly α absorption is strong and broad. These systems are thought to arise on sightlines which pass through galactic disks (see Figure 2.2[B]). However, their true nature is still under investigation (see e.g. Wolfe et al. 1995). There are numerous strategies for discovering damped Ly α systems. Among the most widely used is the method to select absorption features with a certain equivalent width threshold (see Section 2.2.2). A common threshold is 5 Å which corresponds to H I column densities of $\geq 5 \times 10^{19} \text{cm}^{-2}$. Especially for large redshift of $z > 3$ the Ly α forest often contaminates the damping wings and the central position of the Ly α profiles is more securely determined via the observed redshifts of metal lines outside the Ly α forest region (Wolfe et al. 2005).

2.2.1 Observed line profiles

The observed spectrum is a convolution of the true spectrum and the so-called instrumental profile. The observed flux at a given wavelength is:

$$F(\lambda) = \int_0^{\infty} T(\lambda') R(\lambda - \lambda') d\lambda', \quad (2.1)$$

where $T(\lambda')$ is the true spectrum at wavelength λ' and $R(\lambda - \lambda')$ is the response function of the spectroscope at a wavelength distance of $(\lambda - \lambda')$ from the line centre. For an ideal spectroscope the instrumental profile would be the Fourier transform of an equidistant spaced set of delta functions (the grate), modulated by the Fourier transform for a single aperture (the spectrograph's slit). This convolution has a major impact on the line shape, since it limits the minimal width of a spectral feature. For knowingly narrow lines, a first estimation of the instrumental broadening can be made by measuring the FWHM¹ of that line. Any later fitting procedure needs the instrumental broadening parameter to determine how much of a line feature is due to instrumental effects rather than the intrinsic line width, Doppler broadening and other broadening mechanisms. The instrumental profile is usually described as a Gaussian distribution:

$$I(\lambda) = I_{\max} \cdot \exp \left[- \left(\frac{1}{2} \frac{\lambda - \lambda_c}{\sigma_\lambda} \right)^2 \right], \quad (2.2)$$

with λ_c as centre of line. The direct relation between the FWHM and the standard deviation σ of a Gaussian distribution is:

$$\sigma_\lambda = \frac{\text{FWHM}}{2\sqrt{2 \ln 2}}, \quad (2.3)$$

σ is usually expressed in velocity units.

$$\sigma_v = \frac{\sigma_\lambda}{\lambda_c} c = \frac{\text{FWHM}}{2\sqrt{2 \ln 2}} \cdot \frac{c}{\lambda_c}. \quad (2.4)$$

The Maxwell-Boltzmann distribution corresponds to the most probable speed distribution in a collisionally-dominated system consisting of a large number of non-interacting particles in which quantum effects are negligible. Since interactions between the molecules in a gas are generally quite small, the Maxwell-Boltzmann distribution provides a good approximation of the conditions in a gas. The most probable velocity b of the Maxwell-Boltzmann distribution is given by.

$$b = \sqrt{\frac{2kT}{m}}. \quad (2.5)$$

There are three parameters of a known line to be gained from an absorption spectrum: The redshift z , the column density N and the Doppler width b . The redshift is connected to the restframe wavelength of the corresponding transition via the simple relation:

$$1 + z = \frac{\lambda_{\text{observed}}}{\lambda_0}. \quad (2.6)$$

¹full width at half maximum

λ_0 is the rest wavelength of that specific line in the rest frame where the absorption took place. The strength of an absorption feature depends on two parameters. The oscillator strength of that line, i.e. the probability of the corresponding transition and the number of atoms taking part in the absorption. The determination of the actual local density is impossible due to the great difficulties to measure interstellar let alone intergalactic distances accurately and the non-homogeneous distribution of matter along the line of sight of which we have no information. Instead the column density is defined as the integral over the line of sight:

$$N = \int n_i ds, \quad (2.7)$$

where n_i is the number density of the absorbing atoms or molecules, or rather those occupying the lower initial level of the specific transition. That integral is evaluated over the pathlength ds along the line of sight. As a result the column density describes the total number of absorbing molecules (in our case) per unit area over the full distance between source and observer.

The b parameter is not subject of such a direct approach. As mentioned above it emerges from stochastic motion.

The physics behind an absorption line

Assuming I_ν as an intensity of a beam of radiation passing through the unit area per time interval, frequency ν and solid angle, the change of intensity can be written as

$$dI_\nu = -\kappa_\nu I_\nu ds + \varepsilon_\nu ds, \quad (2.8)$$

where κ_ν and ε_ν are then absorption and emission coefficients, respectively. The optical depth τ_ν is defined by

$$\tau_\nu = \int \kappa_\nu ds. \quad (2.9)$$

The resulting intensity reaching an observer through a region of total optical thickness $\tau_{\nu tot}$ is given as:

$$I_\nu(\text{observer}) = I_\nu(0)e^{-\tau_\nu} + \int_0^{\tau_{\nu tot}} \frac{\varepsilon_\nu}{\kappa_\nu} e^{-\tau_\nu} d\tau_\nu. \quad (2.10)$$

The integral part takes possible emission into account. Neglecting it we can express the optical depth in terms of atomic constants in SI units:

$$\tau_\nu = \frac{\pi e^2 c}{4\pi \epsilon_0 m_e c^2} N f_{ij} \phi(\nu) = r_e \pi c N f_{ij} \phi(\nu), \quad (2.11)$$

and r_e being the classical electron radius $e^2/4\pi\epsilon_0 m_e c^2 \approx 2.8179$ fm. f_{ij} is the formerly mentioned oscillator strength of the transition $i \rightarrow j$.

$\phi(\nu)$ is the line profile function. It is a nontrivial function of the distance from the line centre ν_c . Several physical processes contribute to its shape. One factor is the natural line broadening due to finite lifetime of each energy level resulting in an intrinsic line width. This part of the line profile is described by the Lorentz profile, also known as damping profile:

$$L(\nu) = \frac{\gamma}{4\pi^2(\nu - \nu_c)^2 + \frac{\gamma^2}{4}}. \quad (2.12)$$

γ is the full half-intensity width. In case of absorption in intergalactic matter γ qualifies the natural broadening.

Another factor of the overall line profile is of course the Doppler broadening caused in part by thermal velocities and in part by possible micro turbulent velocities of the absorbing molecules. The Doppler profile in case of a Maxwell-Boltzmann velocity distribution is described by:

$$D(\nu) = \frac{c}{\nu_c b \sqrt{\pi}} \times e^{-\left[\frac{c(\nu - \nu_c)}{b\nu_c}\right]^2}. \quad (2.13)$$

The broadening or Doppler parameter b consists of a thermal and the turbulent component:

$$b = \sqrt{\frac{2kT}{m} + b_{\text{turbulent}}^2}. \quad (2.14)$$

The true profile function $\phi(\nu)$ is attained by convolving the line shapes due to natural and Doppler broadening, Lorentz profile (see Equation 2.12) and Doppler profile (see Equation 2.13), respectively:

$$\phi(\nu) = \int L(\nu - \nu') \otimes D(\nu') d\nu'. \quad (2.15)$$

The finally observed spectrum depends on the convolution of this true line profile function $\phi(\nu)$ and the instrumental profile as given in Equation 2.1. However, this accurate method of describing the flux of an absorption feature is very consuming in terms of computing power. Some plausible considerations reduce the complexity significantly. Near the centre of a line, where the Doppler profile is much wider than the damping profile, the Doppler core dominates clearly and the optical depth as in Equation 2.11 can be simplified to:

$$\tau_\nu = \sqrt{\pi} r_e N f_{if} \frac{c\lambda_c}{b} \times e^{-\left[\frac{c(\lambda - \lambda_c)}{b\lambda_c}\right]^2}. \quad (2.16)$$

For relatively small column densities (as we face them for lines of molecular hydrogen), the lines remain rather narrow and the area covered by the line increases proportionally to the column density; such a line is said to be positioned on the linear part of the so-called curve of growth (see next Section). At sufficiently

large column densities, however, the line centre becomes optically thick, and the growth in line strength with column density slows considerably. At even higher column densities, the rate slightly increases again, as the natural broadening in the by now saturated line leads to the appearance of the so-called damping wings, where the Lorentz profile dominates and becomes apparent. The Doppler profile falls off from the central frequency ν_0 as $\exp[-(\Delta\nu/\Delta\nu_D)^2]$ with $\Delta\nu = |\nu - \nu_0|$ and $\Delta\nu_D = \sqrt{2}\sigma_v\nu_0/c$ for an assumed Gaussian velocity distribution. The natural or damped absorption profile falls off with $1/(\Delta\nu)^2$ and at a certain $\Delta\nu$ the probability for the damped absorption exceeds the probability for absorption in the Doppler profile.

2.2.2 Equivalent width and curve of growth

As mentioned in the last section, the area covered by a line profile in a spectrum is of some interest and contains quite some information in itself. The so-called *equivalent width* defines that area as:

$$W_\lambda = \int \frac{F_\lambda(0) - F_\lambda}{F_\lambda(0)} d\lambda. \quad (2.17)$$

For practical reasons the flux F_λ is defined in wavelength terms here. The integral is evaluated over an entire absorption line. An rectangular area of height 1 and a width equal to a specific equivalent width will have the same area covered as the spectral line with that equivalent width. The equivalent width is independent of

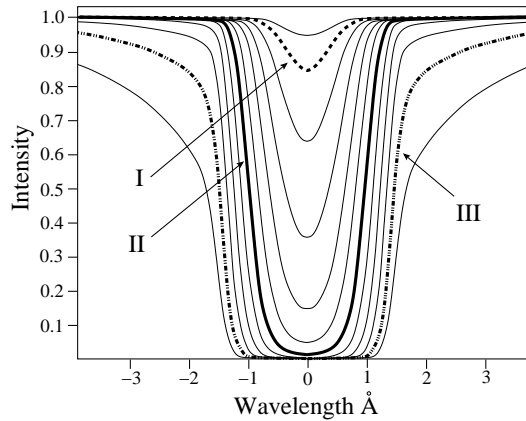


Figure 2.5: Series of synthesised line profiles with increasing column density. The marked profiles I (*dotted*), II (*solid*), and III (*slash-dotted*) correspond to different stages of the curve of growth.

the line shape and another valuable advantage is that it can even be obtained in

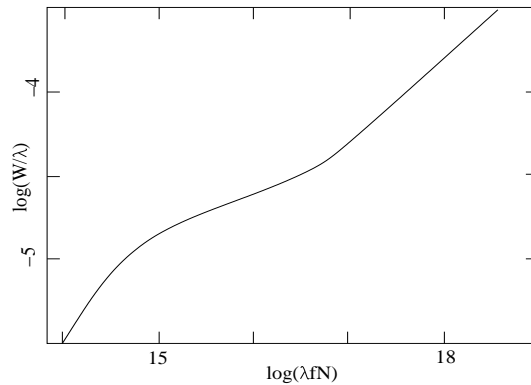


Figure 2.6: Theoretical curve of growth corresponding to a Voigt profile over a large range of column densities.

spectra with not fully resolved lines. It is independent of the instrumental resolution since it merely represents the fraction of energy removed from the spectrum by an absorption line – a quantity unchanged by instrumental broadening. So W_λ can be obtained even if no Voigt or other line profile can be fitted and thus N and b cannot be determined accurately.

In Figure 2.5 a series of synthesised ideal absorption line profiles with different column densities is plotted. The intensity is normalised. In an optically thin gas, the equivalent width of an absorption line is proportional to the number of atoms in the lower level of that transition. Profile (I) in Figure 2.5 is an example for such an optically thin line. The line profile is actually a Gaussian profile. For Line (II) the column density is significantly higher and the intensity of that absorption line in the centre is practically zero. The line is *saturated*. Increasing the column density further will make no difference at all to the central intensity, and have only little impact on the equivalent width. Thus the graph of equivalent width versus column density, the curve of growth, will no longer be proportionally increasing but will be almost constant. The *curve of growth* as diagrammed in Figure 2.6 is a graph showing the increase of the equivalent width of an absorption line with the number of atoms producing that line.

To gain the profile (III) in Figure 2.5 even more molecules along the line of sight were added. Although the central depth does not and cannot become any deeper, the wings of the profile start to add to the equivalent width, so that the curve of growth increases again, although slightly less strong than during the optically thin case.

The curve of growth can be separated into three stages: at first, the equivalent width increases linearly with the column density of the absorber. Then there will be a part in which it is scarcely increasing after all and finally a third stage of reduced but yet present increase. Fig 2.6 also illustrates,

that the line shape itself changes with the column density. In the optically thin case it can be described as "all core and no wings" and is well approximated by a mere Gaussian profile, whereas at high column densities it becomes "extensive wings, with narrow core", best described by the Lorentzian profile mentioned above. The classic three-stage curve of growth is exhibited for the Voigt profile in which the Gaussian and Lorentzian contributions are of comparable influence. In the case of optically thin absorption lines, the line shape can be well described by a Gauss function. The relation between the equivalent width and that Gaussian profile fit to the normalised spectrum can then be simplified to:

$$W_\lambda = A_0 \int_{-\infty}^{+\infty} \exp \left[-\frac{(\lambda - A_1)^2}{2A_2^2} \right] d\lambda = \sqrt{2\pi} A_0 A_2. \quad (2.18)$$

A_0 is the amplitude of the Gaussian distribution and A_2 is its width. A_1 is the line centre. In praxis that integral is evaluated over several line widths only, since the gaussian distribution drops quickly in the outer areas and contributes little to the overall covered area.

For very weak absorption features with optical depth $\tau \ll 1$, the equivalent width is practically linearly proportional to the column density and thus independent of the broadening parameter b :

$$W_\lambda \approx \frac{\pi e^2}{m_e c^2} \cdot f \lambda_0^2 N. \quad (2.19)$$

The classical curve of growth depends heavily on the line-independent nature of thermal broadening. If one knows the line formation temperature and has observations with very good signal-to-noise ratio, one line will give a reasonable estimate of the fractional abundance of the lower state, and with known ionisation state the fractional abundance of the species. However, often neither the temperature nor the oscillator strength nor the signal-to-noise is available. Then, one uses as many lines as possible to construct an empirical curve of growth and then compare it to theoretical curves to gather information on the involved parameters as was done in this thesis.

2.3 Molecular Hydrogen H_2

The first detection of H_2 in the interstellar medium was performed by Carruthers (1970) with a rocket-born ultraviolet spectrometer. Later, with the **COPERNICUS** satellite, the far-UV absorption bands of H_2 were observed in the galactic disk towards several bright stars with a low visual extinction. The full Lyman bands were first recorded at the poles of Jupiter via the **GALILEO** orbiter and since 1999 the far ultraviolet spectroscopic explorer **FUSE** is detecting hydrogen in space, covering the range of the strong Lyman and Werner absorption bands.

2.3.1 Occurrences of intergalactic H_2

H_2 is the most abundant molecule in the universe and plays a fundamental role in many astrophysical contexts. It is found in all regions where the shielding of the ultraviolet photons, responsible for the photo-dissociation of H_2 , is sufficiently large. Except in the early universe, most H_2 is thought to be produced via surface reactions on interstellar dust grains, since gas-phase reactions are too slow in general. The H_2 formation mechanism is not yet fully understood. Direct observations of H_2 are difficult since electronic transitions occur only in the ultraviolet – as described in the following section – to which Earth’s atmosphere is opaque. UV satellites like **COPERNICUS** were only suited for bright nearby objects and could not provide the necessary resolution. Only at great distances and hence with a large redshift these spectra are shifted into the visual band. Another problem is the narrow range of conditions under which H_2 forms. The required dust grains that allow for the forming of molecular hydrogen can easily obscure the molecular hydrogen as well.

Molecular hydrogen is quite abundant in our galaxy. Its abundance is usually expressed as the fraction $f(\text{H}_2) \equiv 2N(\text{H}_2)/[2N(\text{H}_2)+N(\text{H I})]$. Savage et al. (1977) found a correlation in our galaxy of $f(\text{H}_2) \geq 10^{-2}$ for $N(\text{H I}) > 4 \times 10^{20}\text{cm}^{-2}$. A threshold of 5 Å for the equivalent width in the search for DLA systems, as mentioned above, corresponds to $N(\text{H I}) \geq 2 \times 10^{20}\text{cm}^{-2}$ and thus a fraction of $f(\text{H}_2) > 10^{-2}\text{cm}^{-2}$ would be expected for most of the DLA systems. Albeit the observed $f(\text{H}_2)$ in distant DLA is much lower than that. The low H_2 content in DLA in contrast to our galaxy can be explained by their comparably low dust contents. The fraction of molecular Hydrogen can be described as the ratio of its formation on dust grains and its photodissociation by UV-photons via $f(\text{H}_2) = 2Rn/I$ where I is proportional to the intensity of UV radiation and R is proportional to the dust-to-gas ratio κ . A low $f(\text{H}_2)$ in DLAs could then be attributed to a low dust content, and thus a low κ . Such a correlation was indeed found by Petitjean et al. (2002).

2.3.2 Energy levels of H₂

As a first approach to the energy levels of any diatomic molecule we may use the Born-Oppenheimer approximation (BOA) which implies that the electronic, vibrational and rotational energies of a molecule are completely independent of each other and can be evaluated separately:

$$E_{\text{total}} = E_{\text{electronic}} + E_{\text{vibration}} + E_{\text{rotation}}.$$

It should already be mentioned that the fraction of the single terms to the total level energy decreases in this order by a factor of ≈ 1000 each (Demptröder 2000).

Rotational transitions are in the microwave range.

Vibrational transitions are in the infrared range and electronic transitions in the UV band. Thus for each electronic transition, there are vibrational bands and as a substructure of those, rotational bands in the spectrum.

It also should be noted that a mere rotation spectrum is shown in dipole approximation only by molecules with a permanent electric dipole moment, and vibrational transitions require a change of dipole during motion as well. Electronic spectra on the other hand are shown by all molecules and then show additional vibrational and rotational bands since changes in the electron distribution are in principle accompanied by a dipole change.

Thus homonuclear molecules like H₂, which show no detectable mere rotation or vibration-rotation spectra, do in fact give an electronic spectrum and show vibrational and rotational structures in their spectra.

This is essential for this research since part of the electro-rotational-vibrational spectrum at about 1000 Å rest wavelength is redshifted into the visible range. To be precise, there are dipole-forbidden quadropolic rotational-vibrational transitions, but their strength is low and those transitions cannot be expected to be seen in quasar absorption spectra.

Electronic spectra

The hydrogen molecule contains two electrons, each contributed by one of the atoms. In the groundstate both electrons will occupy the lowest orbital – in this case $1s\sigma_g$ and by the Pauli principle, they must form a singlet state. Obviously both electrons are σ electrons and the state is thus $^1\Sigma$. The complete expression for the ground state is: $(1s\sigma_g)^2 \uparrow\downarrow ^1\Sigma_g^+$. The subset g states the even² symmetry of the orbital, while the $+$ indicates the symmetry of the wavefunction.

The two first excited states are $^1\Sigma_u^+$ and $^1\Pi_u$. Transitions are not shown from the lowest triplet state since this is the continuous one as one can see in Fig 2.7. In that state molecules dissociate immediately. The energy level shown for this

²German: gerade = even, ungerade = odd

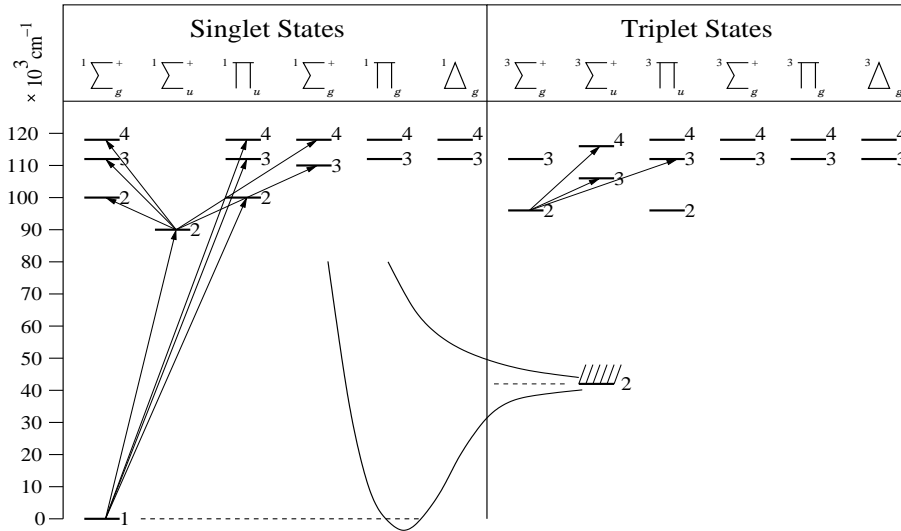


Figure 2.7: The singlet and triplet energy levels of the hydrogen molecule; one electron only is assumed to undergo transitions, the other remaining in the $1s\sigma$ state. The curves correspond to the energy in relation to the internuclear distances for the bonding and antibonding orbitals. The dashed line on the right marks the continuum limit.

state is the dissociation limit. This state (pictured hashed) naturally extends continuously from this limit to the top of the diagram. $\Sigma \leftrightarrow \Sigma$ are referred to as Lyman-transitions, while $\Sigma \leftrightarrow \Pi$ are called Werner-transitions, shortened to L and W respectively in line identifiers. The Lyman bands and the Werner bands connect the electronic ground state to excited states of singlet and *ungerade* symmetry in a dipole-allowed transition. They are the most prominent features in the H_2 spectrum. T. Lyman was the first to assign a spectrum for the $1^1\Sigma_u^+ - 1^1\Sigma_g^+$ system (Lyman 1904). In 1926 the $1^1\Pi_u - 1^1\Sigma_g^+$ was described by S. Werner.

vibrational spectra

In the approximation of a simple harmonic oscillator we get for the energy levels:

$$E_v = \left(v + \frac{1}{2} \right) \bar{\omega}_{\text{osc}} \text{ cm}^{-1},$$

v being the vibrational quantum number and

$$\omega_{\text{osc}} = \frac{1}{2\pi c} \cdot \sqrt{\frac{k}{\mu}} \text{ cm}^{-1},$$

the classical oscillation frequency dependent on the *reduced mass* as $\mu^{-\frac{1}{2}}$. The theoretically possible transitions are

$$E_{v \rightarrow v+1} = \omega_{\text{osc}},$$

whatever the initial v is. A mere vibrational spectrum will occur in heteronuclear molecules only.

In a typical identifier of a spectral line, the vibrational quantum number of the upper state is given.

Rotational spectra

The permitted energy values – or rotational energy levels – are calculated for any molecule by solving the Schrödinger equation for the system.

Assuming a rigid diatomic molecule of the atom masses m_1 and m_2 at the relative distance $r_0 = r_1 - r_2$, the moment of inertia around the centre of gravity ($m_1 r_1 = m_2 r_2$) is defined by $I = m_1 r_1^2 + m_2 r_2^2$. This can be written as:

$$I = \frac{m_1 m_2}{m_1 + m_2} r_0^2 = \mu r_o^2. \quad (2.20)$$

$\mu = \frac{m_1 m_2}{m_1 + m_2}$ is referred to as the *reduced mass* of the system. The Schrödinger equation leads to the following expression for the rotational energy levels allowed to the rigid diatomic molecule:

$$E_J = BJ(J + 1); J = 0, 1, 2, 3, \dots$$

J is the rotational quantum number that allows only certain discrete rotational energy levels to the molecule and B_i is the rotational constant for H₂ (Herzberg 1950):

$$B = \frac{h}{8\pi^2 I_C} = 60.8 \text{ cm}^{-1}. \quad (2.21)$$

Of greater interest in respect to spectra is the difference of those energy levels:

$$E_{J \rightarrow J+1} = 2B(J + 1). \quad (2.22)$$

As we can see with Equations 2.20–2.22 rotational transitions are proportional to μ^{-1} . Rotational transitions follow the selection rule $\Delta J = \pm 1$. Transitions with a $\Delta J = J' - J'' = +1$ form the so called R-branch, and $\Delta J = -1$ the P-branch in a rotational-vibrational electronic spectrum, where ' and '' refer to the upper and lower states, respectively. The Q-branch ($\Delta J = 0$) cannot occur in $\Sigma \leftrightarrow \Sigma$ transitions and thus we only observe it in the Werner transitions.

However, for homonuclear molecules there will be no dipole component change during mere rotation and hence no interaction with radiation.

Unlike with vibrational quantum numbers, line identifiers usually contain information on the rotational quantum number of the final state.

A line identifier of L3P1 for example would indicate a transition in the Lyman Band ($\Sigma \rightarrow \Sigma$) with an initial vibrational number of 3 and a P-branch transition ($\Delta J = -1$) hence resulting in a state with a rotational quantum number of 1. Unfortunately there is no real agreement on that and in some works L3P2 will be used as identifier for the very same electro-rotational-vibrational transition as it is more consistent to give upper state quantum numbers for both, vibrational and rotational levels. It is more convenient though to use the mentioned convention (see e.g. Banwell 1966).

The validity of approximations

The above described approximations merely give a basic idea of the calculations. For more detailed calculations there is to consider the fact that there typically are up to 100 vibrations during one rotation, resulting in a variable nuclear distance and thus a non-constant moment of inertia. Also, at higher rotational levels there is a resulting centrifugal force additionally increasing mean nuclear distance. The assumption of a harmonic oscillator is a rough one but serves here well to display the basic energy levels involved and their dependency on the reduced mass μ . This simple approach gives the following results:

$$\begin{aligned} \text{vibrational transitions} &\sim \mu^{-1} \\ \text{rotational transitions} &\sim \mu^{-\frac{1}{2}} \end{aligned}$$

Electronic transitions are not dependent on the reduced mass. However, they are required for any vibrational and rotational transitions.

2.4 How to measure a possible variation of μ ?

The latest value of the proton-to-electron mass ratio has been measured with a relative accuracy of 2×10^{-9} by Mohr and Taylor (2005) and equals $\mu_0 = 1836.15267261(85)$. The precision reached by today's laboratory experiments rules out considerable variation of μ on short time scales but cannot yet exclude a change over cosmological timescales on the order of 10^{10} years. Additionally the possibility of different proton-to-electron mass ratios in widely separated regions of the universe cannot be rejected. The method to constrain a possible variation of μ as applied in this thesis and described in greater detail in this section was first suggested by Varshalovich and Levshakov (1993).

2.4.1 Sensitivity coefficients K_i

As described in Section 2.3.2, electronic, vibrational, and rotational excitations of a diatomic molecule depend differently on its reduced mass μ . To a first approximation, these energies are proportional to μ^0 , $\mu^{-\frac{1}{2}}$, μ^{-1} , respectively. Hence each transition has an individual sensitivity to a possible change in that reduced mass. This can be expressed by a sensitivity coefficient.

$$K_i = \frac{d \ln \lambda_i}{d \ln \mu} = \frac{\mu}{\lambda_i} \frac{d \lambda_i}{d \mu}. \quad (2.23)$$

A first approximation of these coefficients can be obtained by comparing transitions of molecular hydrogen with deuterium or tritium. Transitions with equal rotational and vibrational quantum numbers have different energies for H_2 and deuterium, or tritium. Recently new experimental data on molecular hydrogen and deuterium level energies were obtained by sophisticated laboratory measurements by Hollenstein et al. (2006). W. Ubachs was so kind to provide these data prior to publication. Since H_2 and D_2 classically only differ in mass, K_i can be computed via Equation 2.23 for each transition using line data of H_2 and deuterium. Of course this is a simplified approach. Figure 2.8 shows a comparison between the values calculated with this method in this thesis and recently recalculated coefficients. As can be seen they are in rather good agreement for the longer wavelengths or lower vibrational levels, respectively. Reinhold et al. (2006) recently refined the calculations of K_i . In first order they can be expressed by the Dunham coefficients Y_{kl} of the ground and excited states. With $\mu_n = \frac{m_e \mu}{2}$, Equation 2.23 leads to:

$$K_i = -\frac{\mu_n}{\lambda_i} \frac{d \lambda_i}{d \mu_n} = \frac{1}{E_e - E_g} \left(-\frac{\mu_n d E_e}{d \mu_n} + \frac{\mu_n d E_g}{d \mu_n} \right). \quad (2.24)$$

The computations for the energies of the excited and ground state, E_e and E_g , respectively are the same as for the energy levels of H_2 . Starting with the BOA

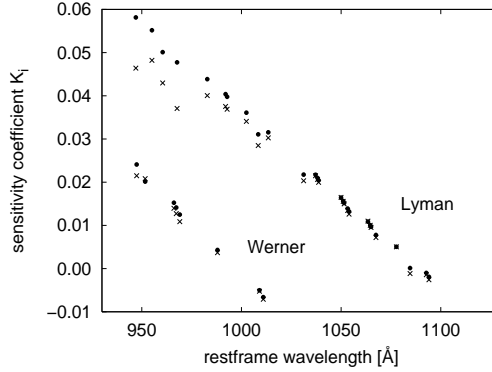


Figure 2.8: Sensitivity coefficients as obtained by comparison of H₂ and D₂ (*filled circles*) and latest calculated values for K_i (*crosses*).

based on the semiempirical approach the energy levels can be expressed by the Dunham formula (see Dunham 1932):

$$E(v, J) = \sum_{k,l} Y_{kl} \left(v + \frac{1}{2} \right)^k [J(J+1) - \Lambda^2]^l; \quad \Lambda^2 = \begin{cases} 0 & \text{for Lyman} \\ 1 & \text{for Werner} \end{cases} \quad (2.25)$$

However, the Dunham coefficients Y_{kl} cannot be calculated directly from the level energies due to strong mutual interaction between the excited states as well as avoided rotational transitions between nearby vibrational levels. For the first time the more complex non-BOA effects are taken into account in the work of Reinhold et al. (2006). Their recent laboratory measurements of the level energies of molecular hydrogen allowed for a reliable enhancement of the BOA approximation. The influence of the inclusion of the Bohr-shift and adiabatic corrections is shown in Figure 2.9 (*right*) in percentage compared to prior sensitivity coefficients as obtained by Varshalovich and Potekhin (1995).

2.4.2 Distinguish cosmological redshifts from variation of μ

With K_i from Equation 2.23, the restframe laboratory wavelengths λ_i^0 are related to those in the quasar absorption system λ_i via

$$\lambda_i = \lambda_i^0 (1 + z_{\text{abs}}) \left(1 + K_i \frac{\Delta\mu}{\mu} \right), \quad (2.26)$$

with z_{abs} as the redshift of the absorbing system. This can be expressed in terms of the individual redshift of each measured H₂ component:

$$z_i = z_{\text{abs}} + bK_i. \quad (2.27)$$

According to Equation 2.27 the redshift of each H₂ feature can be distinguished between the intrinsic redshift of the absorber and an additional component due to a possible variation in μ . Equation 2.27 describes a simple linear equation with a gradient of

$$b = (1 + z_{\text{abs}}) \frac{\Delta\mu}{\mu}. \quad (2.28)$$

A linear regression of the redshift of each H₂ line z_i and its individual sensitivity coefficient K_i will yield the redshift of the absorbing DLA system and $\Delta\mu/\mu$ during the epoch between $z = z_{\text{abs}}$ and today. It is worth noting that in the case of non-zero variation the redshift of the absorber is not identical to the mean redshift of all observed lines as can be derived from Equation 2.27.

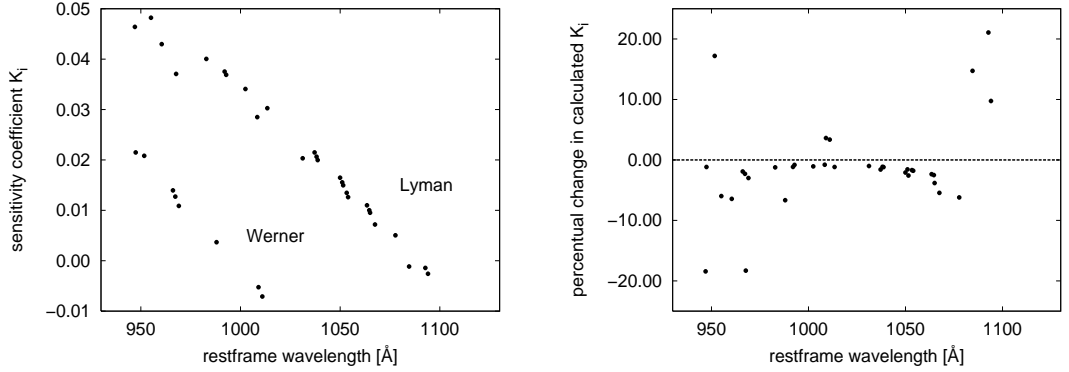


Figure 2.9: Sensitivity coefficients of observed lines in the Lyman and Werner band (*left*) and recent refinement of K_i given in percentages (*right*).

3 Methods and Data

3.1 Observation

3.1.1 The Quasar Q0347-383

The source of the analysed spectrum is a bright quasi-stellar radio object (QSO) with a visual magnitude of $V = 17.3$ mag at a redshift of $z = 3.23$ (Maoz et al. 1993). Its signature Q0347-383 contains the rounded spherical coordinates – a right ascension (RA, or α) of 3h47m and a declination (δ) of -38.3° . This is the identifier of the "Fundamental-Katalog" 4.0 calibrated to 1950 but still being widely used. The precise position dated to 2000 as stated in the fifth fundamental catalogue is α 03h 49m 43.68s, δ $-38^\circ 10' 31.3''$.

Q0347-383 was discovered by Osmer and Smith (1980). The Quasar absorption line spectra were obtained with the Ultraviolet and Visual Echelle Spectrograph (UVES) spectrograph at the Very Large Telescope (VLT) of the European Southern Observatory (ESO) in Paranal, Chile. The slit was 0.8 arcsec wide resulting in a spectral resolution of $R \approx 53,000$ over the wavelength range 3300Å–4500Å. The average seeing¹ during observation was about 1.2 arcsec. Before and after the exposures for each night, Thorium-Argon calibration data were taken. An overall of nine spectra were recorded with an exposure time of 4500 seconds each between January 8th and January 10th 2002 for the ESO program 68.A-0106(A). All spectra were taken with grating 430 and the blue "Pavarotti"-CCD with 2x2 binning. Later on the data were reduced manually by Mirka Dessauges-Zavadsky from Geneva Observatory in Jan 2004 to achieve maximum accuracy. The ESO Ambient Conditions Database² includes measurements of the environmental parameters at the Paranal ESO observatory and shows no significant changes in temperatures during or inbetween the exposures that could lead to shifts between the separate observations.

¹Astronomical seeing refers to the blurring and twinkling of astronomical objects caused by turbulence in the Earth's atmosphere. The astronomical seeing conditions on a given night at a given location describe how much the Earth's atmosphere perturbs the images of stars as seen through a telescope. The most common seeing measurement is the diameter (technically Full Width Half Maximum) of the seeing disc (the point spread function (PSF) for imaging through the atmosphere) (Buscher et al. 1995).

²<http://archive.eso.org/eso/ambient-database.html>

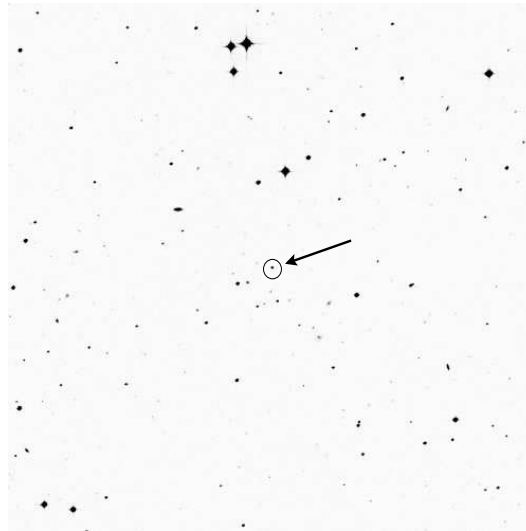


Figure 3.1: Colour inverted and contrast enhanced photograph taken in the Blue-Band (J) covering a $14' \times 14'$ area. Q0347-383 is marked by a circle and arrow. Original image from Space Telescope Science Institute (STScI).

3.2 Data reduction

3.2.1 Binning of observed data

The detector resolution is naturally finite. The stringest limitation is the pixel size of the CCD³. All photos hitting the area of such a CCD-pixel are binned to the same spatial resolution. The CCD used is composed of a 2048×4096 matrix of such pixels, each pixel with a size of $15 \mu\text{m}$. So the practically continuous spectrum of dispersed light is projected onto the CCD and mapped or so-called binned to the separate pixels of the CCD. It is quite common to interconnect some pixels and thus have a higher photon count resulting in a higher sensitivity and signal to noise ratio, though cutting in half the resolution. Here, a 2×2 binning was used. The resulting spectrum was corrected for earth's orbital motion along the line of sight and the measured wavelengths are converted to their accordant vacuum wavelengths. The binning itself leads to a discontinuous data output of the final reduced spectrum. Each pixel corresponds to a specific central wavelength. Due to the geometry of the spectrograph and the reduction procedures, the wavelength steps between each successive pixel differ with the wavelength.

³charge-coupled device

3.2.2 Coadding spectra from different observation runs

A possible method to gain a higher signal-to-noise ratio is to add up several observed spectra of the same object – the so-called coaddition. Usually an observation is split up into shorter exposures to keep instrumental errors small and to ensure constant environmental conditions during exposure and to equal out cosmics. These separate spectra can be added up for a better statistic and thus a better signal-to-noise ratio. Assuming Poisson statistics to describe the photon count of the detector, the photon noise increases with the square root of the number of detected photons.

$$\sigma_{\text{photons}} = \sqrt{N_{\text{photons}}}. \quad (3.1)$$

Hence, coadding all nine spectra results in a photon noise that has decreased by a factor of 3. However, the error of each data point is not merely due to photon noise and the true gain in the signal-to-noise ratio must be accepted to be considerably smaller. To add up spectral data, the bins of each spectrum must be rearranged to match the central wavelength of the corresponding bins in the other spectra. This must be done carefully to ensure an unchanged global and local flux. The common practise is to rebin the data into slightly larger bins usually with equidistant wavelength steps in-between them. The accuracy of this method depends highly on the model used to ensure an unchanged local flux and on the relative wavelength calibration of the data. However, the coaddition leads to a slightly lower spectral resolution and introduces a new correlation between pixels. Another drawback is the possible impact on the line shapes in case the different spectra are slightly shifted against each other or show other independent systematic errors that may not necessarily cancel out via coaddition. A cross-correlation analysis usually reveals systematic shifts between two compared spectra. The weighted coaddition considers the different signal-to-noise ratios. The flux \tilde{F}_i of the coadded spectrum is computed via:

$$\tilde{F}_i = \frac{\sum_k (F_i / \sigma_{ik}^2)}{\sum_k 1 / \sigma_{ik}^2}, \quad \tilde{\sigma}_i = \sqrt{\sum_k \sigma_{ik}^2}, \quad (3.2)$$

with the sums evaluated over $k = 1 \dots N$, the number of coadded spectra.

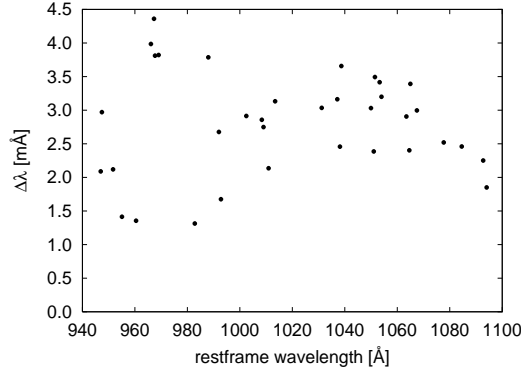


Figure 3.2: Changes in mÅ in restframe wavelengths $\Delta\lambda = \lambda_P - \lambda_A$ between data by Philips (2006) and Abgrall (1993), "P" and "A" respectively.

3.3 Transition frequency tables for H₂

For some time the only available precise data on oscillator frequencies and for this study more important restframe wavelengths for molecular hydrogen were those computed by Abgrall and Roueff (1989). Later, a refined table of wavenumbers was published (Abgrall et al. 1993). The claimed accuracy lay at about 1mÅ corresponding to $\approx 4\text{mÅ}$ for the observer's frame in this case. In 2004 J.Philip et al. conducted high-resolution laser-spectroscopy to gain precise transition frequencies in the Lyman and Werner bands (Philip et al. 2004). A strong test on the accuracy of transition frequencies is to compare the differences between the rotational branches $P(J+2)$ and $R(J)$ (see Section 2.3.2). They should match the calculated ground state rotational splittings, which are accurately known (see Jennings et al. 1984). The achieved accuracy is stated as $< 0.01 \text{ mÅ}$. In the framework of this analysis the restframe wavelength can thus be assumed to be exact. Due to experimental restrictions on the UV laser range the transition frequencies were obtained only for a subset of the lines detected in the Q0347-383 spectrum. The differences between the high precision experimental data and the previously calculated restframe wavelengths, however, were too massive to combine them (see Figure 3.2). As can be seen the new data have a throughout positive offset. A publication in 2006 completed the data on the Lyman frequencies. The new data tables include all observed and selected H₂ lines. W.Ubachs made those data available prior to publication via private communication so they already could be used in the present study. Figure 3.2 illustrates the increasing uncertainty in calculations for shorter wavelengths or rather higher vibrational levels. The stated errorbars of $< 0.01 \text{ mÅ}$ for the new data are below the size of the data points in the plot.

3.4 Fitting data

3.4.1 χ^2 Fitting

The main concept of fitting data to a model is based on minimising a function that expresses the deviation between the data and the model – the so-called figure-of-merit function. The parameters of the model can then be adjusted to minimise the merit function and thus to obtain the best-fit parameters. With real data, however, an uncertainty of each data point is introduced preventing an exact fit to the model even if the model is correct. Furthermore the merit function may not have only one minimum. The appropriate evaluation of a fit thus goes beyond judging the quality of the fit but also needs a statement on the certainty of the fit at hand being the best possible set of parameters in the underlying parameter space. A fitting procedure should provide the best-fit parameters, their error-estimates and finally a statistical measure of the goodness-of-fit to judge the quality of the former values.

The general problem is to describe a set of n data points $(x_i, y_i), i = 1 \dots n$ with individual known errors σ_i by a model parameterised by m parameters $y(x) = y(x; a_1, \dots, a_m)$. The task then is to find a set of model parameters that describes the data best. For this purpose a function is defined that measures the deviation between the data and the model with the current set of parameters. If each data point has its individual known standard deviation σ_i the so-called "chi-square" or χ^2 describes that discrepancy:

$$\chi^2 \equiv \sum_{i=1}^n \left(\frac{y_i - y(x; a_1, \dots, a_m)}{\sigma_i} \right)^2. \quad (3.3)$$

The χ^2 assumes that the measurement errors are normally distributed. For a more detailed discussion of this see Section 6.2.4. The derivative in respect to the model parameters of Equation 3.3 must equal zero at the minimum. The necessary criterion is to find a parameter set for which the following equation holds true:

$$0 = \sum_{i=1}^n \left(\frac{y_i - y(x_1)}{\sigma_i^2} \right) \left(\frac{\partial y(x_i; \dots, a_k, \dots)}{\partial a_k} \right), k = 1, \dots, m. \quad (3.4)$$

This is straight forward solvable for linear models. Non-linear models require an iterative approximation procedure to deliver the best-fit set of parameters though.

3.4.2 Fitting procedures

Since the model for fitting a theoretical line profile to observed data is indeed not linear the possible procedures are described in more detail. As first step an initial set of parameters is evaluated. Most fitting procedures depend on a reasonable

manually selected set to bring the iterative algorithm on the right track so to say. The most naive approach is to fit a line feature by a model based on the initial set and then vary each free parameter independently to find a minimum in the objective function describing the discrepancy between observation and fit.

This approach is of course unpractical, since the number of necessary calculations of the synthetic profile increases exponentially with each free parameter. Also the parameter range and resolution must be set sufficiently large to ensure a global minimum. Furthermore a reasonable range must be manually selected to assure that the covered parameter space does include the best-fit parameters.

The common approach is thus to collect information about the local topography of the objective function by calculating its partial derivatives for each free parameter. This ensures a far more rapid convergence to a nearby minimum. This method (as implemented in the Levenberg-Marquardt algorithm for example) has the deficiency of relying on the initial parameter set, since in a straight forward implementation of this algorithm, possibly only a local minimum is found – depending on the situation not necessarily the global minimum. The first iteration step is based on the initially selected parameter set. Afterwards a second set of parameters is evaluated. The Levenberg-Marquardt algorithm interpolates a gradient of χ^2 in respect to the free model parameters and thereby ascertains the "direction" in the parameter space towards the local minimum. The second derivative of χ^2 , more generally the Hessian matrix⁴ delivers the appropriate stepsize for each parameter. Depending on the implementation, this stepsize is scaled additionally to match the required needs. A new parameter set based on the information of the direction and the selected stepsize is evaluated and in case of a smaller χ^2 value used as fulcrum for the next iterationstep. The additional scaling is used to increase the resolution in the parameterspace with each iteration step. The iteration is completed when the change between successive χ^2 values falls below a certain threshold value. The value of the minimal χ^2 depends on the number of effective degrees of freedom. $r = n - m$ with n being the number of fitted data points and the number of free model parameters m . It is obvious that any reasonable fit requires $n > m$. An value independent on the number of data points or the selected model is described by the normalised χ^2 :

$$\chi_{\text{norm}}^2 = \frac{\chi^2}{r}. \quad (3.5)$$

In the ideal case the final value of χ_{norm}^2 reaches unity. That would mean that the total deviation between model and data equals the measurement errors of the data as can be deduced from Equation 3.3. A value below 1 thus indicates an invalid model or overestimated individual errors σ_i .

The approach applying evolutionary algorithms, such as the code implemented by Quast et al. (2005) that is used here, is based on stochastics (also see e.g.

⁴The Hessian matrix is the square matrix of second partial derivatives of a scalar-valued function.

Hansen and Ostermeier 2001). The principle is similar to the one described above but instead of a manual first guess of initial parameters, several sets of random initial parameters are computed automatically over a parameter range that needs merely rough preselection. The most successful of those build the centres of other groups of random, yet less wide spreaded sets of parameters and so forth. This stochastic approach can additionally be fine-tuned by adjusting the expansiveness of each successive group of random parameters in both the parameter space and in quantity. With a sufficiently widespread cluster of parameter sets, theoretically the global minimum will always be reached. In practice a compromise must be found between computing time and success in reaching the global minimum. Its drawback is of course its inefficiency in terms of computing power and the need to check up the final fit on physically reasonable parameters. However, the principle of evaluating multiple groups of parametersets independently of each other allows for consequent parallel computing.

The element of randomness requires a full completion of the iterative process. Whilst the Levenberg-Marquardt algorithm usually converges rather soon towards the final parameters the evolutionary procedure can only give reliable results after all branches of parameter groups are evaluated. Some principle problems of redundancy in parameter sets for complex models have yet to be overcome as well. In praxis two or multiple line profiles whose parameter spaces significantly overlap can cause the algorithm to lock up on rare occasions. The dynamical scaling towards regions with small Hessian matrix to gain higher resolution is implemented by an increasingly smaller scattering of random parameter sets for successive child populations of parameter sets.

This fitting program uses a simplified pseudo-Voigt-function to generate the synthetic line profiles. As described in Section 2.2.2 for weak lines a mere gaussian profile would suffice since natural line broadening has no noticeable impact on the line shapes.

3.4.3 Simultaneous fit vs. coadded fit

The fitting program used has the ability to fit several lines simultaneously to one subset of free parameters. Individual parameters can be cross referenced to each other and the code is under the constraint to find one best joint fit for these parameters. This feature is of great convenience since several line parameters as broadening width or column density are usually shared by a whole group of lines and do not differ among each other. This concept has even been expanded to fit several separate spectra simultaneously. So even for overlapping wavelength regions, the continuum and for example the redshift are fitted locally but the line width is fitted to all participant spectra and lines.

This method appears to be superior to a rough prior coadding of spectra. Many errors a coarse coaddition might introduce can be avoided this way, since there is

no need to rebin the data. A further rebin would introduce a stronger correlation of pixels. However, such a correlation is known to have no impact on the mean result (Aitken 1934). A χ^2 minimisation procedure does rely on independent data points though. The concept of simultaneous fit has the advantage of taking physical conditions into account in form of further restrictions on the degrees of freedom.

3.4.4 Background considerations

An accurate estimate of the true continuum of a spectrum is essential for a good fit of an absorption line. Especially for optically thin lines the determined column density is very sensitive to variations in the continuum fit. Particularly in damped Lyman- α systems (DLA) at large redshifts there hardly is any unblended continuum detectable in the range of H₂ absorption due to the Lyman- α forest. There are numerous techniques and strategies to gain a reliable estimation of the true continuum despite its contamination.

A rather generic approach is specific to pure absorption spectra and assuming that the data points with the highest photon count contribute to the continuum, since there are no emission features. Therefore a polynomial function of low order is fitted iteratively to a selected subset of data points above a certain threshold. This threshold is increased or rather the range between Flux_{min} and Flux_{max} (if there are some spikes or cosmics in the spectra) is narrowed with each iteration step until a minimum variance or the predefined minimum number of selected data points is reached. This method is only applicable though when a reasonable amount of undisturbed continuum emission is present in the wavelength range of interest.

Another way of dealing with the continuum is to construct it manually. The curve of the estimated continuum is drawn or based on some interpolation points. The continuum level simply is set at the upper end of an absorption line feature to disregard all influences of other lines nearby. Dealing with the continuum in this manner yields a great uncertainty that only a curve of growth analysis can reveal. Albeit this is one of the few options to deal with heavily contaminated and partially blended lines at all.

A refinement of the latter approach is to not only fit the one line of interest and border it by an artificial continuum but to fit a series of lines with free parameters to match the disturbed measured flux. The actual line of interest is then embedded into a group of lines that are used to fit the surrounding flux level. The true continuum, however, needs to be estimated but for a larger less alternating environment. In some cases the extra lines may disturb the shape of the measured main component and this procedure needs special supervision.

In this work, the continuum is fitted by the code together with the lines. The fit is based on the flux adjoining the line feature. In some specific cases with

problematic line surroundings, several free lines are fit as well to get a proper continuum. However, this mostly was the case whenever the H₂ line was positioned on a flank of a saturated damped Lyman- α line and those cases usually were sorted out anyway. The accuracy of the continuum fit increases significantly by the option of simultaneous fitting. All molecular hydrogen lines observed at the same rotational level should have identical physical properties, as in column density and line width. This constrains the uncertainty of the continuum since the resulting column density has to be consistent with the simultaneous fits of the more secure continuum regions. However, a mere χ^2 consideration to evaluate the quality of the fit is invalid, since the model of a single line does not describe the observed flux sufficiently.

3.5 Simulations

To test the accuracy of fits without a clean continuum a code to generate synthetic spectra was written and several simulations were performed. For that purpose a synthesised molecular hydrogen line was placed in the region of the wing of a broad almost saturated synthesised Lyman- α feature as illustrated in Figure 3.3. To match the conditions of the combined observed quasar spectra, a signal-to-noise of about 90 containing Gaussian and Poisson photon noise were synthesised. The observed signal to noise with ≤ 70 lies slightly below that, but the intention of this simulation was also to reveal systematic effects rather than statistical errors. The position of the H₂ feature was shifted through the broad Lyman- α line in 100 steps. For each position a number of 100 synthesised spectra were generated and each time the molecular hydrogen line along with the atomic component was fitted. For each fit the absolute deviation of the fitted H₂ position and its true position as was fed into generation of the synthetic spectra is plotted against the true position. The idea was to determine the accuracy and stability of the fitting algorithm and its dependency on the line environment. Figure 3.3 (*right*) and Figure 3.4 (*right*) show the results with the mentioned settings. As can be seen the fits with the H₂ component placed in a clean continuum result in an constant average error of several mÅ. However, the amplitude of the error distribution increases rapidly towards the centre of the central component. In the core area the optically thin H₂ feature is practically not observable. As the simulation shows, up to a certain point the fitting accuracy of the H₂ line is not affected by its position on the outer wing of the broad Lyman- α line. For Figure 3.4 (*left*) the same method was used to generate the spectra but instead of fitting both components and the continuum simultaneously, the continuum is fitted by a third grade polynomial to the flux enclosing the H₂ line without fitting the Lyman- α component explicitly. This is a dramatic difference since for that approach no information on the environment of the fitted line is needed. The physical origin of the continuum contamination is not taken into account

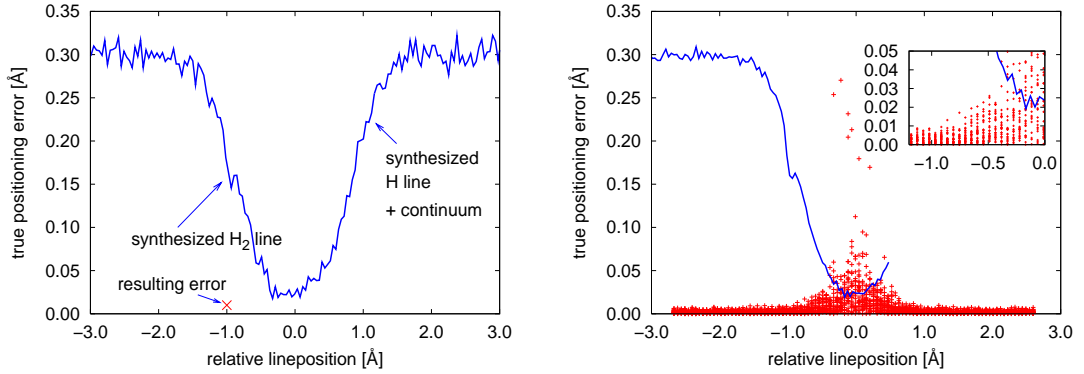


Figure 3.3: Series of fits of synthesised spectra. On the left an exemplified case and on the right an overview with a blow up of the central region.

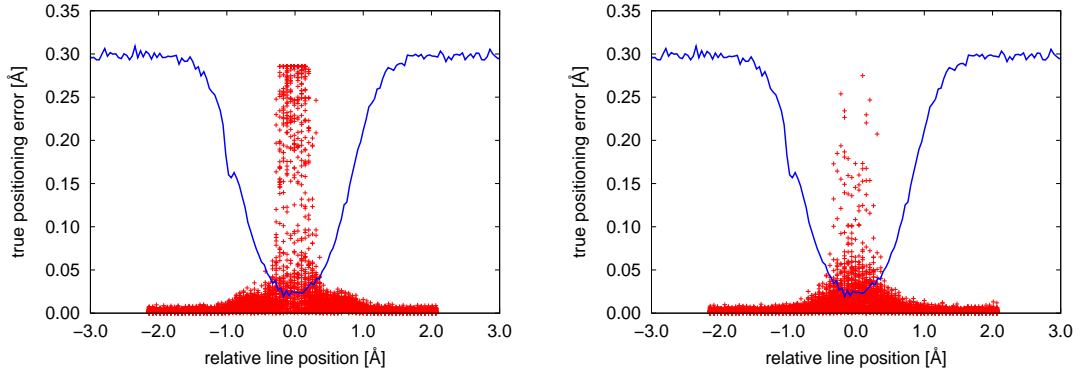


Figure 3.4: Results of simulated fits with $S/N=90$. Comparison of single component fit (*left*) and two component fit (*right*).

here. As Figure 3.4 shows, the quality of the fits obtained via polynomial fit (*left*) and the two component fit (*right*) is quite similar in the clean continuum area and up to a certain point on the wing of the broad Lyman- α feature. This is a beneficial result since in the observed spectra it would be impossible to divide the continuum contamination into single components that could be fitted simultaneously. However, the position of the H_2 lines is critical for the quality of the fit and they cannot easily be determined. Figure 3.4 also reveals the different behaviour towards the centre of the main component. The apparent cut off on the left plot is due to that fact that a limit of 0.30 \AA as error of position was set up to which a line can be considered fitted at all. The comparatively low equivalent width of the H_2 line makes it practically indistinguishable from noise near the core for the one component fit. The method of polynomial continuum fit is clearly inferior near the core of the main component in this simulation but an error of more than 0.05 \AA is unacceptable for this analysis in general. A more detailed discussion will follow in Chapter 6.

4 Data analysis

4.1 Identification of H₂ lines

To gain a better signal-to-noise ratio the nine spectra were coadded to identify H₂ lines (see Section 3.2.2). A preliminary inspection of the Q0347-383 spectrum revealed over 80 absorption features at positions that would indicate an H₂ line. The H₂ lines are mostly noticeable by their narrow line profiles and generally low equivalent width. The observed spectrum has an instrumental resolution of 5.6 km s⁻¹. With Equation 2.14 a line width of 6 km s⁻¹ already corresponds to a temperature of more than 4000° Kelvin for doppler broadened H₂ lines. A lower excitation temperature is to be expected for molecular Hydrogen. The observed width of the H₂ features can thus be expected to be given by the spectral resolution. The fit of the line shape or a curve of growth analysis will later give information about the physical broadening parameter.

After the redshift of the DLA was determined, the H₂ lines were identified by a linelist of Abgrall et al. (1993). At that point the most precise data available. To validate the manual identification a synthesised spectrum of the strongest H₂ transitions that were to be expected, was generated and compared with the quasar data. Not all of the identified lines appeared to be suitable for further analysis because of H I contaminations. In fact only 39 observed absorption features remained after careful selection. Of the excluded lines some were sorted out due to

- too strong contamination,
- a position on a too steep or saturated H I line,
- blending with other H I or even H₂ lines as the curve of growth revealed.

4.2 Curve of growth

The curve of growth easily reveals blended lines and also allows for an estimation of the line widths and column densities independently of the result of the main fitting procedure. Furthermore it can operate as an autonomous test of the general fitting procedure. The curve of growth could also have been produced from the fitted data via Equation 2.19 as described in Section 2.2.2. For a more independent enquiry the curve of growth was constructed with equivalent widths gained

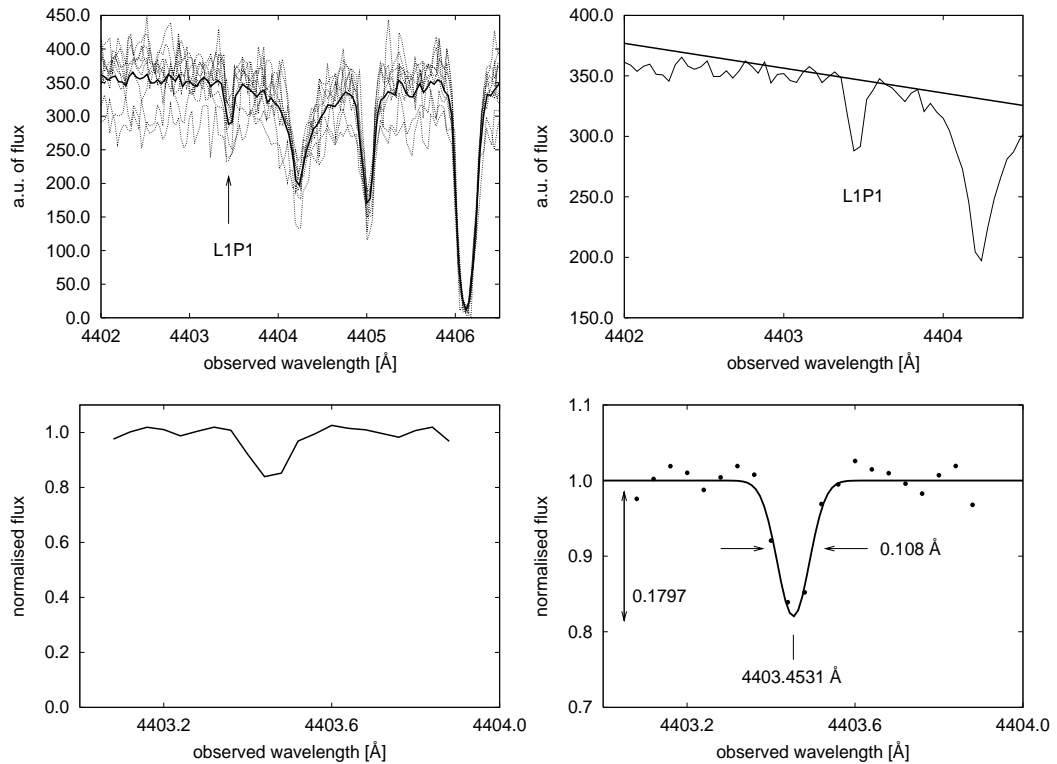


Figure 4.1: The single steps for the curve of growth for the L1P1 H_2 line. Coadding the nine spectra (*top left*), selecting a linear model for the continuum by hand (*top right*), rectifying the coadded spectrum and normalising it (*bottom left*), fitting a Gaussian profile via Levenberg Marquardt (*bottom right*) with the FWHM, amplitude and centre given in the plot.

of a simple gaussian fit of each line feature following Equation 2.18. For this task a stand alone C-code was written that handles most of the necessary steps. At first the nine observed spectra were rebinned and coadded – the formerly described problems that arise from that procedure have no significant influence on the measured equivalent width of a line and are negligible. Then a previously selected area of a line feature was rectified and normalised. The normalised line feature was fitted with a Gaussian line profile using the Levenberg-Marquardt algorithm that was implemented from the Numerical Recipes (Press et al. 1992). Figure 4.1 illustrates the single steps for L1P1 as exemplar. Fitting the normalised profile by a Gauss profile yields the parameters for FWHM, amplitude and position (in this example 0.108 \AA , 0.1797 and 4403.4531 \AA , respectively). A later simultaneous fit via the main fitting routine yields a line centre of $4403.4517 \pm 0.0038 \text{ \AA}$. The equivalent width for L1P1 can now be calculated to $W_\lambda = 0.0243 \text{ \AA}$.

This procedure was applied to all selected molecular hydrogen lines, but for each

rotational level separately. A set of theoretical curves of growth was then computed using a mere Doppler profile, since the molecular hydrogen lines are optically thin and all lines happen to be mostly in the linear area of the curve of growth as can be seen in Figure 4.2. In principle the shape and offset of the curve allows to determine both, line width and column density. However, in the part of the curve of growth covered by the measured equivalent widths the values only vary slightly with the line width.

Applying the Levenberg-Marquardt algorithm, a theoretical curve of growth was fitted to each of the rotational levels. This required a numerical determination of its derivative. Figure 4.2 shows the result for all three observed rotational levels. The fitted solid curve corresponds to a broadening parameter of $b = 1.8 \text{ km s}^{-1}$. As comparison curves of growth for $b = 1$ and $b = 3 \text{ km s}^{-1}$ are shown. The scatter of the data does not allow to distinguish the broadening parameters between the rotational levels. All rotational levels fit best to the plotted curve corresponding to $b = 1.8 \text{ km s}^{-1}$. A common broadening parameter b is consistent with a simple model of UV optical pumping which dominates the H_2 rotational populations for an optically thin, homogeneous gas. For the selected lines the fitted curve of growth gives the column densities for each rotational level: $\log N_{J=1} = 14.5$, $\log N_{J=2} = 13.8$ and $\log N_{J=3} = 14.0$. These results will be discussed further in comparison to the main fit results in the next section.

As intended the curve of growth can clearly detect the erroneous fits. The plot shows an example of a blend that was revealed by the curve of growth analysis. The profile of W1R1 shows a significantly higher equivalent width. This indicates a possible blend and in fact this absorption feature is an unresolved blend of W1R1 and W1R0 at restframe wavelengths of 985.6398 and 985.6294 Å, respectively. Both transitions emerge with comparable oscillator strengths (0.033 and 0.069) and thus contribute to the large equivalent width of that absorption feature. The original analysis revealed several similar blends and resulted in the selected subset of 39 H_2 features. The remaining 39 lines are in good agreement with the fitted theoretical curve of growth and the initial assumption of optically thin H_2 lines.

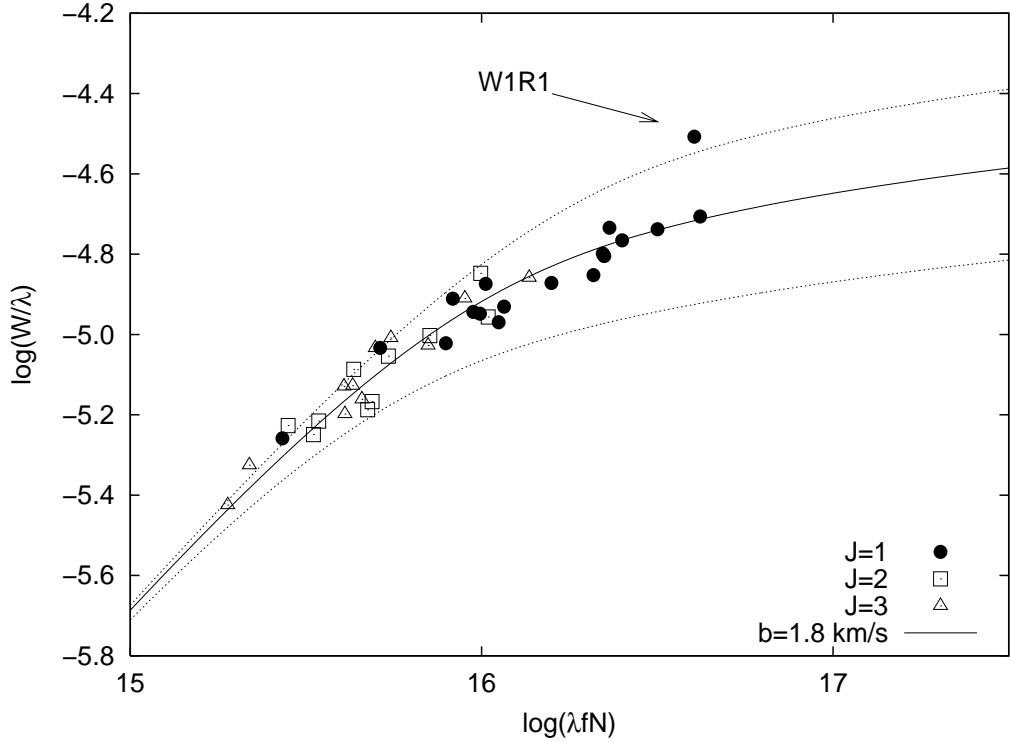


Figure 4.2: Curve of growth for the observed absorption lines. Theoretical curves of growth for $b = 1.8 \text{ km s}^{-1}$ (*solid*) and $b = 1, 3 \text{ km s}^{-1}$ (*dotted*). The marked line W1R1 is sorted out due to its apparent blend with another line.

4.3 Fitting of H₂ features

The selected and verified H₂ lines were fitted with the `rq-edfit` fitting programme by Ralf Quast. The input of the program contained a wavelength range over which the continuum was determined and fitted with a polynomial. The range was selected individually for each line by eye to have the best compromise between clean continuum and number of pixels contributing to it. The grade of the polynomial was manually selected to match the continuum flux. As described in Section 3.4.4 in some cases an additional line was fitted along with the H₂ component to have a better fit to the flux. For those cases the true continuum was fitted via a linear function. This procedure is justified despite the non linear run of the background flux for the whole spectrum (see Figure 2.4 and 2.3). For small wavelength windows, the true continuum can be assumed to meet a linear form. Lines L1R1, L2R1, L5P1, L3R2 and W1Q2 (see Figures 4.7 – 4.8) were fitted with a second component.

In cases of a continuum flux with apparent influences of broad Lyman- α features

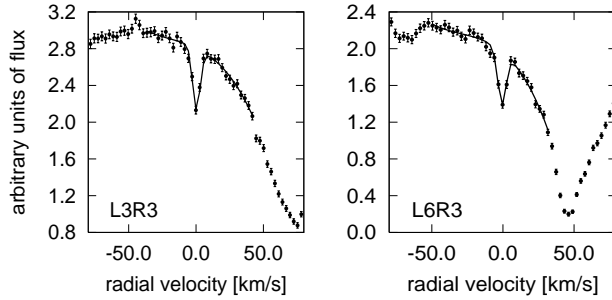


Figure 4.3: Continuum matching via parabolic fit to the observed flux for L3R3 and L6R3.

or general contamination, a parabolic or cubic function was used to fit the background to the observed flux. See Figure 4.3 of L3R3 and L6R3 for an exemplar of a parabolic fit. To gain an optimal fitting result, the lines were fitted in several steps.

4.3.1 A check for possible shifts between the nine observed spectra.

At first fits were performed for each of the nine observed spectra with a low signal-to-noise of $\approx 20 - 30$ separately. For the fits the program's capability to fit one parameter to multiple lines was used to gain stability. Each set with the same rotational quantum number was fitted to conjoin broadening velocity and column density, since these are physical properties expected to be equal for lines of the same rotational state. The range for the common broadening velocity was set to $1.0 - 5.0 \text{ km s}^{-1}$, whereas at first approach a rather huge range for the logarithmic column density $\log N = 12 - 16$ was allowed. The data concerning oscillator strength was acquired from the calculations of H.Abgrall and E.Roueff whereas for the restframe wavelength more precise measured data by J.Philip et al. was used in the final computations (see Section 3.3). The fits give an individual redshift for each H_2 feature. To reveal a possible systematic shift in one or several of the nine separately observed spectra, a mean redshift for the 39 lines in each spectrum was computed. With the assumption that the measured redshifts cluster around the redshift of the absorber z_{abs} it is appropriate to describe the central redshift by the *mean* of the measured redshifts. The mean value of a set of z_i estimates the centre value around which the clustering occurs and is defined as:

$$\bar{z} = \frac{1}{N} \sum_{i=1}^N z_i. \quad (4.1)$$

spectrum	mean z	standard deviation
A1	3.02488	0.00003
A2	3.02490	0.00002
A3	3.02487	0.00002
B1	3.02488	0.00003
B2	3.02493	0.00004
B3	3.02487	0.00003
C1	3.02490	0.00002
C2	3.02488	0.00002
C3	3.02493	0.00003

Table 4.1: Mean redshift of all observed H₂ lines with $J = 1$ for each of the spectra.

The quality of this estimation depends on the shape of the distribution and the convergence in its tails. An expression for the variability around that mean value is the *variance*:

$$\text{Var}(z_1 \dots z_N) = \frac{1}{N-1} \sum_{i=1}^N (z_i - \bar{z})^2, \quad (4.2)$$

which is the square root of the *standard deviation*. Table 4.1 lists the mean values for the measured set of redshifts and the standard deviation for each of the nine spectra. The large deviations render this comparison useless. They can in principle be explained by the low signal-to-noise ratio for the single spectra. Figure 4.4 reveals the origin of the huge deviations. Due to the low signal-to-noise, three lines apparently could not be fitted in all nine spectra and the algorithm failed in some cases. These lines correspond to transitions with rather low oscillator strength and thus allow no stable fit at such high noise levels. For a reliable analysis those three lines with uncertain positioning fit were sorted out. Excluding the lines in question for the computations of the mean value gives Table 4.2: No systematic shift between individual observed spectra is distinguishable. However, it is worth noting that a standard deviation in redshift of about 1×10^{-5} describes all observed H₂ lines of first rotational level with a single central redshift of the absorber. 1×10^{-5} in redshift corresponds to ≈ 10 mÅ in the observed wavelength.

4.3.2 Simultaneous fits for all nine spectra

After the verification of the relative calibration of the different spectra further line fits were conducted simultaneously for all nine spectra. The individual spectra have a rather low S/N-ratio and the fits to a single spectrum can hardly be examined. Figure 4.5 contains the observed flux for each spectrum and an

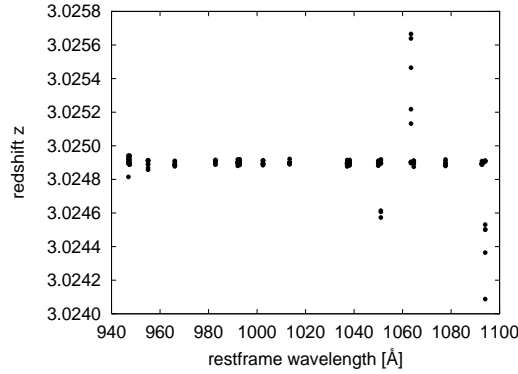


Figure 4.4: Fitted redshift of H_2 features with rotational level $J = 1$ for all nine spectra.

spectrum	mean z	standard deviation
A1	3.024903	0.000012
A2	3.024898	0.000011
A3	3.024895	0.000015
B1	3.024894	0.000007
B2	3.024901	0.000009
B3	3.024904	0.000011
C1	3.024896	0.000011
C2	3.024901	0.000010
C3	3.024902	0.000008

Table 4.2: Mean redshift of reduced set of observed H_2 lines with $J = 1$ for each of the spectra.

exemplary fit of the H_2 line L1R1 in particular. This also is an example of a line that was fitted with an secondary free component to achieve the best fit to the observed flux. For Figure 4.6 all nice spectra were coadded and thus the S/N-ratio is clearly higher. The plotted fit to the line feature is the result of a fit exclusively applied to the coadded spectrum. In principle the results for the fit to the coadded spectrum and those from the simultaneous fits differ. The coadded data was only used for demonstration and identification of H_2 features. The nine individual fits of the observed spectra as in Figure 4.5 differ from each other only in the continuum fit. The other parameters as column density, broadening parameter and the redshift are fitted to a conjoint value that describes all nine spectra best. The spectra are weighted by their individual signal-to-noise ratios. For each of the 39 lines a range of the continuum area was decided and a redshift range manually computed in which the line was to be fitted. After a

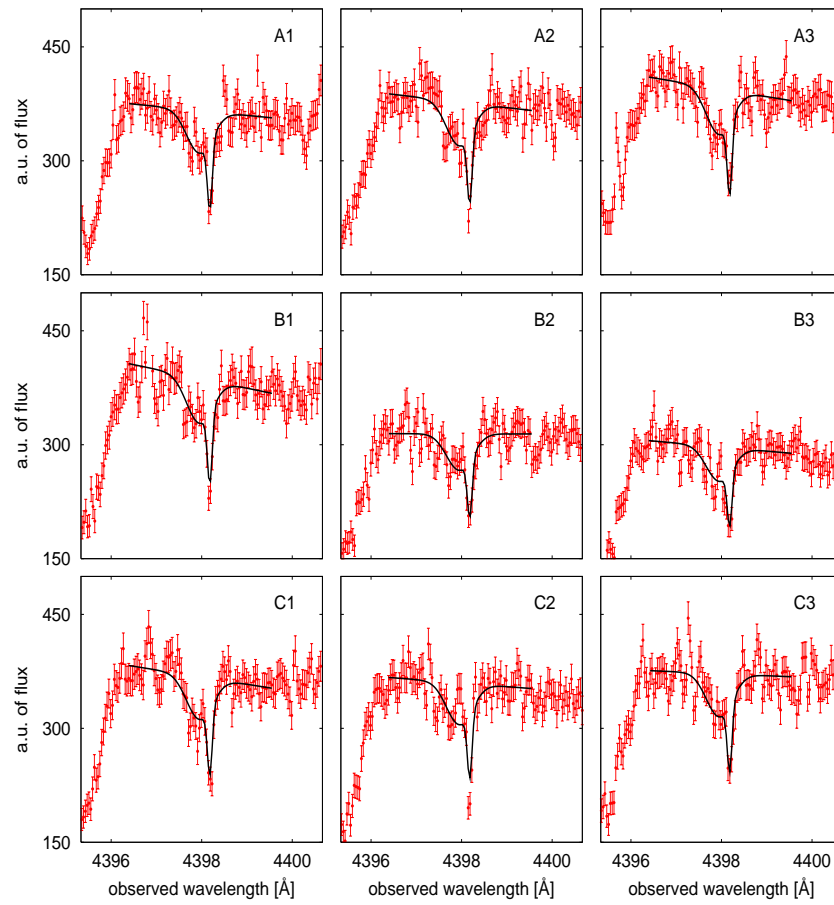


Figure 4.5: Data of all nine separately observed spectra (A1-C3) with errorbars and exemplary fit of L1R1.

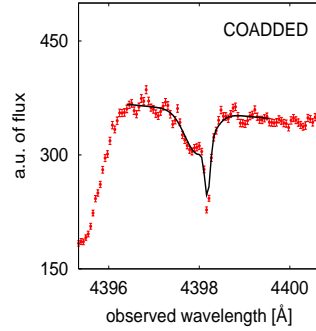


Figure 4.6: Coadded data with errorbars and fit of L1R1.

preliminary run the parameters were refined to allow for a more target-oriented fit. The ascertained redshift of each line was taken as new input for the following fit. The positioning range for each line was expressed in relative velocity to its central redshift. This allows for equally large range in the positioning parameter for all lines. Furthermore a fit in the velocity space simplifies the procedure for the fitting code due to the lower number of relevant decimal places compared to a fit in the redshift-space. In the final run the lines were fitted with a refined velocity range of $\pm 2 \text{ km s}^{-1}$.

Stability of the evolutionary algorithm for the conducted fits

Due to the evolutionary algorithm the fitting procedure depends on a random seed value to start the stochastic spread of initial fitting parameters with. To test the fitting procedure for stability, 100 cycles of the whole fitting with different seed values had been carried out. The results show no deviation at all in the obtained individual redshifts z_i up to the given accuracy of $0.1 \text{ m}\text{\AA}$. Merely the estimated error σ_z of the magnitude $1 - 3 \text{ m}\text{\AA}$ varies by up to $0.5 \text{ m}\text{\AA}$ with varying seed value. The same holds for the fitted broadening velocity and column density. The fits can therefore be considered stable as expected for such one-to-one situations.

4.3.3 Profiles and fits of selected H_2 features

Figures 4.7–4.9 contain the 39 fitted H_2 features, separated by the rotational quantum number $J = 1 - 3$, respectively. Each line is plotted as a fit to the coadded spectrum with its immediate vicinity and thus not identical to the evaluated fits in all aspects (as described in Section 4.3.2). The zero point of the radial velocity on the abscissa corresponds to the measured individual redshift of each line. The ordinate in arbitrary units of flux is scaled differently to illustrate the individual line shapes of the H_2 features. For this purpose a suitable range

rotational level	CoG		Fit	
	b [km s ⁻¹]	LogN	b [km s ⁻¹]	LogN
1	1.8	14.49	1.3 ± 0.2	14.39
2	1.8	13.86	1.4 ± 0.2	13.71
3	1.8	14.00	1.4 ± 0.2	14.00

Table 4.3: Column densities and broadening parameters for the different rotational levels as obtained via curve of growth fit and simultaneous lin-fit.

for the radial velocity of 50 km s⁻¹ was chosen. The different scaling is reflected in the diagrammed size of the error bars as well. Each line is labelled with its line identifier as described in Section 2.3.2. Table 4.3 lists the line parameters in comparison with the values obtained from the curve of growth analysis. The column densities are in good agreement, whereas the the broadening parameters differ significantly. This is probably due to the difficulties in producing a good fit to the b parameter in the curve of growth for optically thin lines. Furthermore the estimated accuracy of the fitting programme to give proper line widths clearly below the spectral resolution of 5.6 km s⁻¹ is not very high. Ivanchik et al. give a Doppler parameter of $b = 1.3 \pm 0.2$ km s⁻¹ for all three rotational levels of H₂ of the same DLA via curve of growth analysis, whereas Levshakov et al. (2002) computed a value of $b = 2.80 \pm 0.45$ for H₂ based on an observation with lower spectral resolution of the same DLA by the method of minimising the obtained χ^2 for simultaneous fits with varying b parameter.

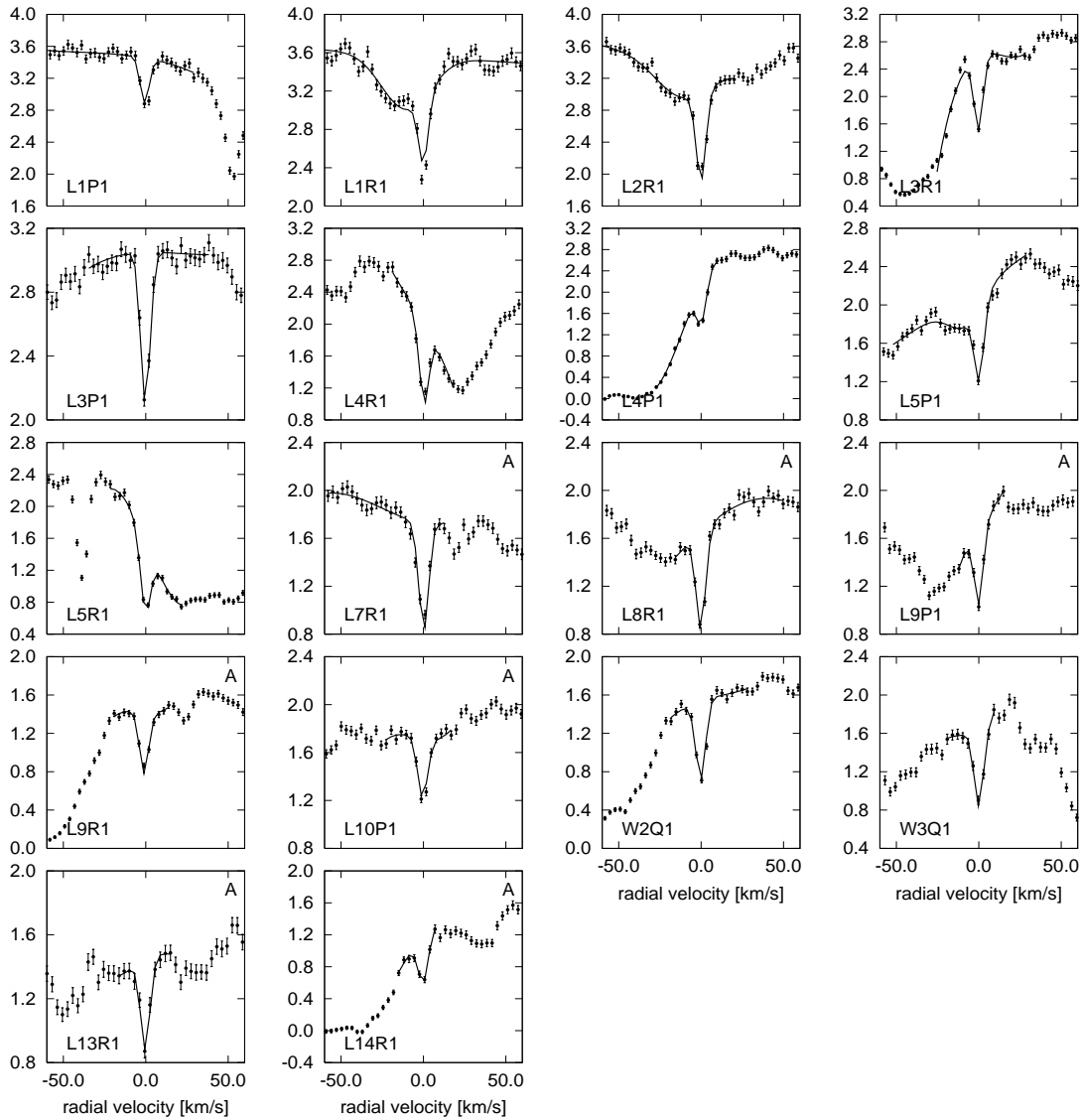


Figure 4.7: Coadded spectrum (*data points with 1σ errorbars*) in arbitrary units of flux and corresponding fits of the 18 selected H_2 lines of the first rotational level $J=1$. Note the adjusted scaling.

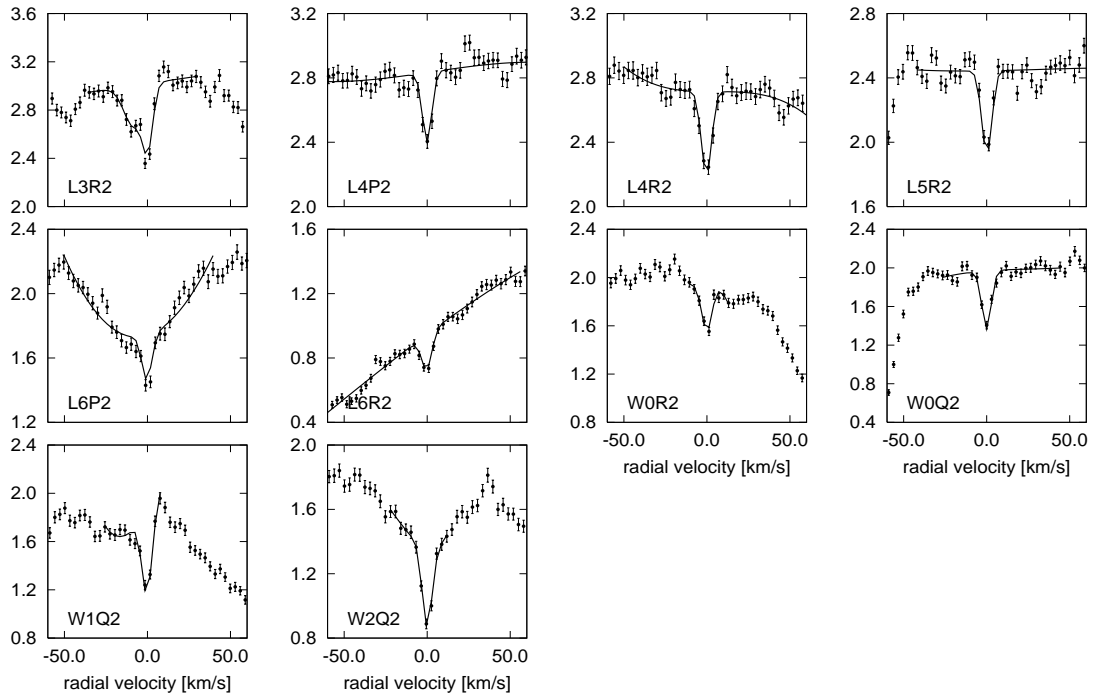


Figure 4.8: Same as in Figure 4.7 but with 10 profiles of second rotational level $J=2$.

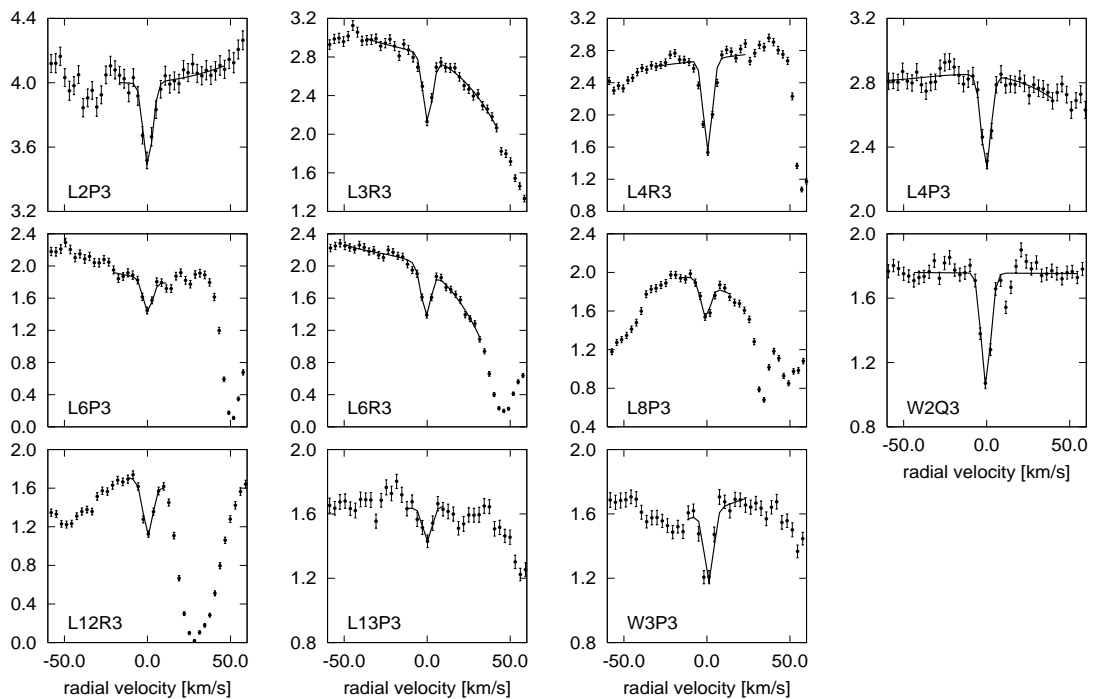


Figure 4.9: Same as in Figure 4.7 but with 11 profiles of third rotational level $J=3$.

5 Results

5.1 Evaluation of the obtained individual redshifts z_i and the corresponding sensitivity coefficients K_i

As described in the earlier chapters all 39 lines were fitted and a corresponding redshift ascertained. The measured redshifts with their obtained standard deviations are not consistent with a single mean redshift at the 1σ level. Accordant to the method described in Section 2.4 the measured redshifts were tested for a possible correlation with the individual sensitivity coefficients. Figure 5.1 shows the resulting plot. The dotted line represents a preliminary linear fit to the data. According to Equation 2.27 the redshift of the absorber does not in principle correspond to the mean redshift, but can be ascertained by the point of zero sensitivity towards possible μ -variation, since at this point the measured redshift equals the cosmological redshift. The ordinate is given in relative redshift with respect to the absorber $z_{\text{abs}} = 3.0248990(13)$. The linear fit corresponding to $\Delta\mu/\mu = 2.1 \pm 1.4 \times 10^{-5}$ was achieved by a linear regression without taking into account the individual estimated errors in the redshift to allow for a comparison with the results of Reinhold et al. (2006) who measured $\Delta\mu/\mu = 2.0 \pm 0.6 \times 10^{-5}$ with the method of an unweighted fit but based on two spectra of quasars. The argumentation behind an unweighted fit is that the dispersion of the experimental points then characterises the true statistical errors. At a 95% confidence level this results in a constraint of the variation to $-0.7 \times 10^{-5} \leq \Delta\mu/\mu \leq 4.9 \times 10^{-5}$. However, a straight forward linear fit to the data turns out to be inappropriate. A more detailed analysis will follow in the next chapter.

Figure 5.2 illustrates the $z_i - K_i$ relation for all three observed rotational levels combined (*top left*) and each of them separately (*top right and bottom*). At first glance there seem to be significant differences in the estimated accuracy of the derived redshifts. Evidently only the first rotational level shows an apparent correlation between redshift z_i and sensitivity coefficients K_i . Table 5.1 gives the mean redshifts \bar{z} for each corresponding rotational level. It is worth noting that the deviation $\sigma_{\bar{z}}$ from the mean value is smaller than the 2σ level of the mean estimated error $\bar{\sigma}_z$.

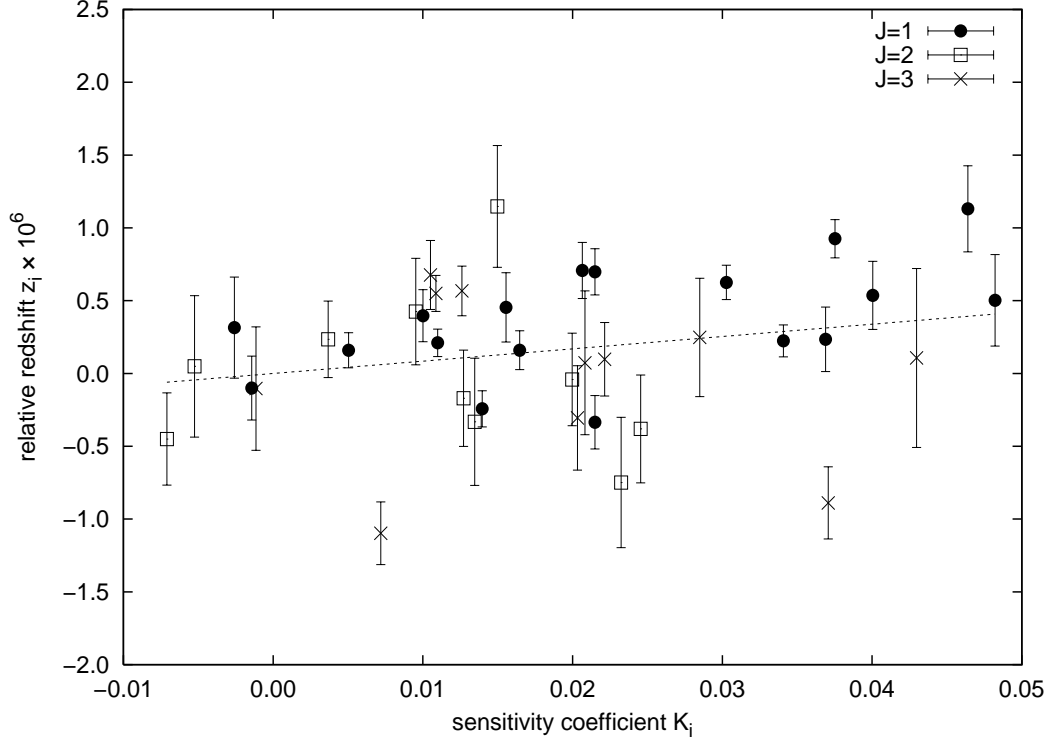


Figure 5.1: Plot of $z_i - K_i$ relation for all observed rotational levels. The Origin of the relative redshift corresponds to $z_{\text{abs}} = 3.024899$. The linear fit (*dashed line*) is consistent with $\Delta\mu/\mu = 2.1 \times 10^{-5}$.

J	\bar{z}	$\sigma_{\bar{z}}$	$\bar{\sigma}_z$
1	3.0249022	3.8×10^{-06}	1.9×10^{-06}
2	3.0248982	5.3×10^{-06}	3.8×10^{-06}
3	3.0248984	5.7×10^{-06}	3.2×10^{-06}

Table 5.1: The mean redshift \bar{z} for each rotational level, along with its standard deviation in comparison to the mean estimated error of the redshift $\bar{\sigma}_z$.

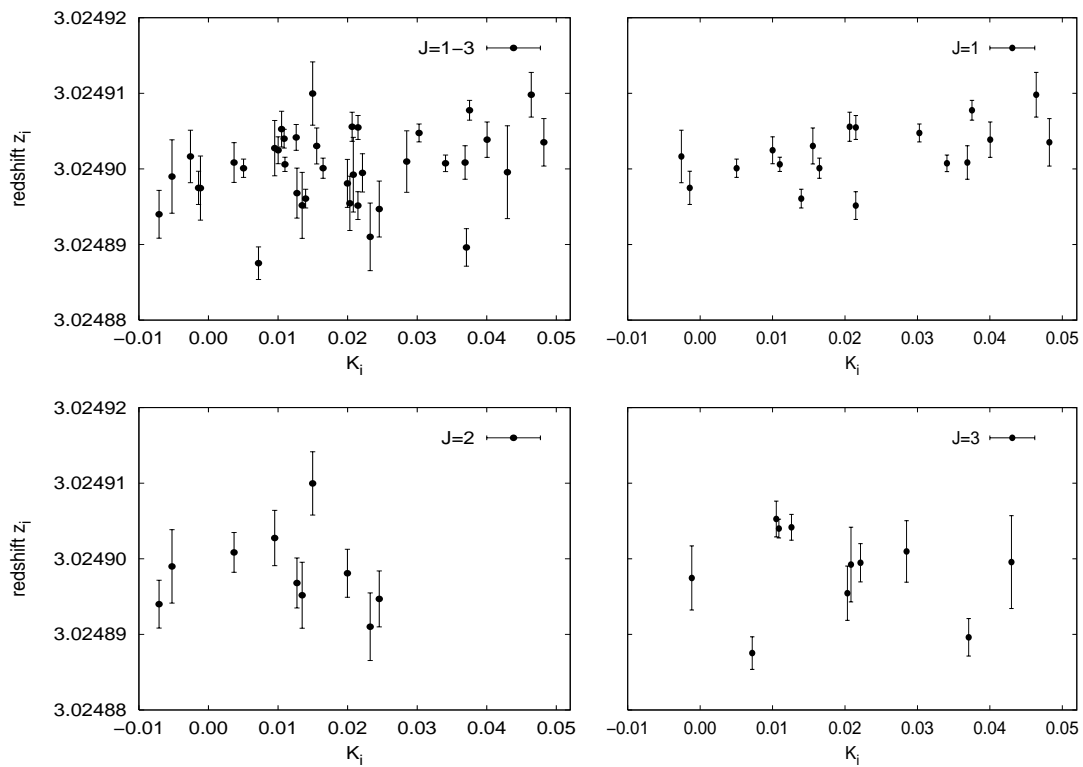


Figure 5.2: $z_i - K_i$ relation with individual redshifts for the whole dataset (*top left*) and separate rotational levels $J=1$ to $J=3$ (*top right and bottom*).

Line ID	f	λ_0	λ_{obs}	$\sigma_{\lambda_{\text{obs}}}$	z_{obs}	K_i
L1P1	0.0020	1094.0520	4403.4517	0.0038	3.0249017	0.00259
L1R1	0.0038	1092.7324	4398.1359	0.0024	3.0248975	0.00143
L2R1	0.0077	1077.6989	4337.6304	0.0013	3.0249001	0.00504
L3R1	0.0120	1063.4601	4280.3212	0.0010	3.0249006	0.01099
L3P1	0.0060	1064.6054	4284.9329	0.0019	3.0249025	0.01001
L4R1	0.0160	1049.9598	4225.9833	0.0014	3.0249001	0.01647
L4P1	0.0076	1051.0325	4230.3039	0.0025	3.0249030	0.01556
L5P1	0.0087	1038.1571	4178.4843	0.0020	3.0249056	0.02064
L5R1	0.0180	1037.1499	4174.4196	0.0019	3.0248951	0.02149
L7R1*	0.0200	1013.4370	4078.9874	0.0012	3.0249048	0.03027
L8R1*	0.0180	1002.4521	4034.7702	0.0011	3.0249007	0.03408
L9P1*	0.0077	992.8097	3995.9606	0.0022	3.0249008	0.03689
L9R1*	0.0180	992.0164	3992.7745	0.0013	3.0249078	0.03753
L10P1*	0.0068	982.8353	3955.8176	0.0023	3.0249039	0.04005
L13R1*	0.0098	955.0658	3844.0477	0.0030	3.0249035	0.04821
L14R1*	0.0190	946.9804	3811.5107	0.0028	3.0249098	0.04640
W2Q1	0.0350	966.0961	3888.4364	0.0012	3.0248961	0.01396
W3Q1	0.0270	947.4219	3813.2836	0.0015	3.0249055	0.02149
L3R2	0.0110	1064.9948	4286.5005	0.0039	3.0249028	0.00953
L4P2	0.0091	1053.2843	4239.3589	0.0046	3.0248952	0.01346
L4R2	0.0140	1051.4986	4232.1872	0.0044	3.0249100	0.01497
L5R2	0.0160	1038.6903	4180.6226	0.0033	3.0248981	0.01997
L6P2	0.0110	1028.1061	4138.0150	0.0046	3.0248910	0.02324
L6R2	0.0180	1026.5281	4131.6675	0.0038	3.0248947	0.02454
W0R2	0.0160	1009.0249	4061.2233	0.0049	3.0248990	0.00525
W0Q2	0.0240	1010.9384	4068.9199	0.0032	3.0248940	0.00710
W1Q2	0.0360	987.9745	3976.4994	0.0026	3.0249008	0.00368
W2Q2	0.0350	967.2811	3893.2066	0.0032	3.0248968	0.01272
L2P3	0.0050	1084.5603	4365.2440	0.0046	3.0248975	0.00115
L3R3	0.0100	1067.4786	4296.4813	0.0023	3.0248875	0.00719
L4R3	0.0130	1053.9761	4242.1528	0.0018	3.0249042	0.01261
L4P3	0.0096	1056.4714	4252.1973	0.0025	3.0249053	0.01051
L6P3	0.0110	1031.1926	4150.4424	0.0037	3.0248954	0.02033
L6R3	0.0170	1028.9856	4141.5636	0.0026	3.0248995	0.02214
L8P3	0.0100	1008.3862	4058.6546	0.0041	3.0249010	0.02849
W2Q3	0.0350	969.0492	3900.3300	0.0012	3.0249040	0.01088
L12R3	0.0230	967.6769	3894.7927	0.0024	3.0248896	0.03707
L13P3	0.0049	960.4506	3865.7172	0.0059	3.0248996	0.04297
W3P3	0.0130	951.6719	3830.3835	0.0047	3.0248992	0.02082

Table 5.2: Parameters of the fitted H₂ lines in order of rotational, electronic and vibrational quantum numbers. The subset of seven lines at rotational level $J = 1$ at high vibrational states with $K_i > 0.03$ are marked with an '*'.

6 Error analysis

6.1 Line fits

As described in Section 3.5 the accuracy of a fitted line position depends on the continuum contamination or rather its position on a wing of a stronger, in DLA-systems saturated Lyman- α component. Near the centre of such a Lyman- α feature, the fitting method has a great influence on the error distribution. For a more detailed analysis the simulations in Section 3.5 were refined to gather information on the resulting error distribution. Again roughly 100 simulations for 100 different relative positions were performed for both fitting methods in question. Figure 6.1 shows the mean true error of the simulation runs as gained from exact comparison (*bold*) and the mean value of the calculated error from the output of the fitting program (*dotted*). The left plot shows the results of the single component fit whereas the right plot shows the mean errors of the two component fit and for illustration a plot of the synthetic spectrum with an exemplary H₂ line. Note the identical scale of both plots. As Figure 6.1 points out, the procedure of fitting a single component only and describing the continuum by rectifying a third grade polynomial fit leads to significantly larger errors in the core area. Also the mean error of line position fits for lines situated near the core region is dramatically underestimated by the fitting program. In the case of the two component fit the mean true error and the error given by the fitting routine match quite well. Great caution was exercised in the selection of H₂ lines to avoid such critical cases. However, it is evidently difficult to evaluate the relative position of a H₂ feature.

In Figure 6.2 the errors of the simulated fits were added up to reveal a possible net shift of the position fit. The results for the two methods differ dramatically. While the two component fit shows no significant overall shift despite the greater uncertainties in the core region, the one component fit produces a major net shift of the fitted line position. A potential shift almost of the order of two magnitudes higher than the average error in clean continuum demonstrates the importance of avoiding lines in such critical positions. The apparent solution – to use a multi component fit and thus to "recreate" the continuum level is only applicable in few cases. The ideal conditions of a single Lyman- α as simulated do not correspond to the observed data. Fitting an arbitrary number of free Lyman- α components in the environment of each H₂ line could also easily result in an shift of the comparatively weak H₂ lines. The only acceptable consequence is to avoid these

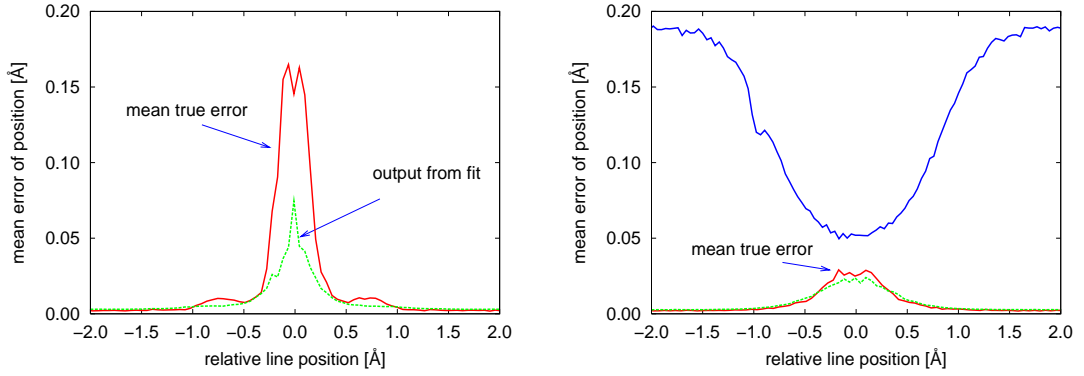


Figure 6.1: Mean value of true error and outcome of the fitting procedure. Comparison of single component fit (*left*) and two component fit (*right*).

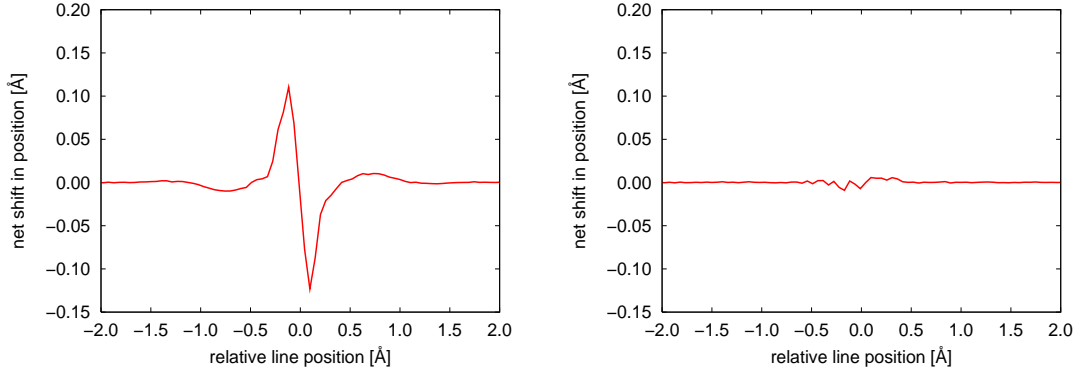


Figure 6.2: Mean shifts of fitted position over a series of fits for the single component fit (*left*) and the two component fit (*right*).

critical lines, since even for the simulated two component fit the individual error in position is unacceptable for the aspired precision.

One cannot assume possible shift caused by this to even out completely at these low statistical totalities. However, they would not mimic a variation of μ since this effect applies equally to all transitions. In general the simulations show that the mean error as estimated by the fitting procedure seems to be rather reasonable for unblended, non-critical lines.

6.2 Significance of detection of variation

As Figure 5.2 on page 44 illustrated the three different rotational levels of H_2 show a very different behaviour. The measured gradient in the linear regression results from the first rotational level alone. To investigate this circumstance further several statistical tests were accomplished.

6.2.1 Pearson product-moment correlation coefficient

The Pearson product-moment correlation coefficient (PMCC) also called *Person's* r is a measure of how well a linear equation describes the relation between two variables. It is defined as:

$$r = \frac{\sum_i (x_i - \bar{x})(y_i - \bar{y})}{\sqrt{\sum_i (x_i - \bar{x})^2} \sqrt{\sum_i (y_i - \bar{y})^2}}, \quad (6.1)$$

and is equivalent to dividing the covariance between the two variables by the product of their standard deviations. The range of r is -1 to 1 , a complete negative correlation and a complete positive correlation, respectively. A zero value of r indicates that the two variables are uncorrelated. For any real data complete correlations cannot be expected. However, the first impression of a very weak correlation (see Figure 5.2) can be quantified. The validity of this analysis depends heavily on the assumption of a mere linear dependency between the two variables, in this case the measured redshift and the sensitivity coefficient. This linear relation is given by Equation 2.27 and independent on a possible variation of $\Delta\mu/\mu$. In fact any discrepancy from a linear relation between z_i and K_i could only be caused by massive errors in the data reduction. Such an analysis may also not prove conclusive when multiple datasets are combined (see for example Reinhold et al. 2006; Ivanchik et al. 2005).

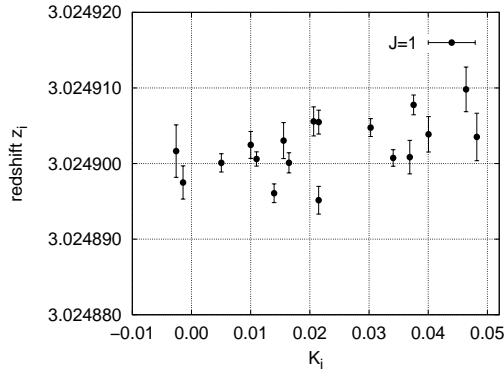
The computed correlation coefficients are listed in Table 6.1. Due to the low number of data points a concluding evaluation of the correlation coefficients would be inappropriate. However, the analysis indicates the very weak correlation of the data. Apparently only the first rotational level contributes to a positive linear correlation at all. A correlation coefficient of the magnitude as in Table 6.1 hint towards a random distribution of the data points. The second and especially third rotational level for themselves do not indicate a positive variation in μ .

6.2.2 Dependency of the result on single lines

A closer examination of the first rotational level (see Figure 6.3) by eye shows that the positive gradient of the linear regression seems to evolve only by the rightmost seven data points. This impression can be confirmed by a correlation test for all

rotational level	r	data points
1	0.29	18
2	-0.16	10
3	-0.62	11
all	0.24	39
subset	-0.08	32

Table 6.1: Correlation coefficients for different datasets

Figure 6.3: z_i - K_i relation for lines with $J = 1$.

data points except those seven lines with $J = 1$. Table 6.1 lists the correlation coefficient of this subset as $r = -0.08$. A result quite consistent with no correlation at all. However, seven data points represent a considerable subset of the total of 39 lines. In Figure 4.7 these seven lines are marked with an A and show no distinctive features that would indicate an erroneous fit. The seven lines (namely L7R1, L8R1, L9R1, L9P1, L10P1, L13R1, L14R1) evidently have a sensitivity coefficient of > 0.03 (see Figure 6.3) in common, they also emerge from high energy transitions (see Figure 2.9). As can be seen from the line identifiers, the seven lines in question all arise from high vibrational levels in the Lyman band. This matches fully with the range where the sensitivity coefficients deviate the most from the Born-Oppenheimer-approximated calculations¹. This is illustrated in Figure 2.9 (*right*). The uncertainties given for the recent values of K_i cannot explain the distinctiveness of this subset, albeit the according computations for the restframe wavelengths depend on the same nonadiabatic interactions not included in BOA. This effect is also reflected in the differences between the calculated and experimentally gathered restframe wavelengths (see Figure 3.2 on page 23).

¹”Changes in K_i rise sharply from < 0.0001 at $v \leq 7$ to -0.005 at $v = 14$.” (from Reinhold et al. 2006)

Spearman Rank-Order correlation coefficient

To quantify the z_i - K_i correlation, a Spear Rank-Order correlation coefficient r_s was calculated. It is a non-parametric measure of correlation – that is, it assesses how well an arbitrary monotonic function could describe the relationship between two variables without making any assumptions about the frequency distribution of the variables. Unlike the Pearson product-moment correlation coefficient, it does not require the assumption that the relationship between the variables is linear, nor does it require the variables to be measured on interval scales. Furthermore it allows to determine the significance of a non-zero correlation. Instead of measured values merely their ranks are compared. In case of discriminative values in N pairs of variables r_s is obtained straight forward by

$$r_s = 1 - \frac{6D}{N^3 - N}. \quad (6.2)$$

$D = \sum_{i=1}^N (R_i - S_i)^2$ is the sum squared difference of ranks R_i and S_i of the variables K_i and z_i , respectively. The idea behind this approach is to bring the two variables in rising order separately and then compare the two ranks of a data pair. For a perfect linearly correlated set D is obviously 0, since for this case both variables always equal in rank. The maximum value of D is reached at a perfect negative correlation. D then equals $N(N^2 - 1)/3$. The ratio of the observed D to its maximum possible value will be 0 in the case of perfect positive correlation, +1 in the case of perfect negative correlation, and +1/2 in the case of zero correlation. To transform that into a range of $-1 \dots +1$ it is doubled and subtracted from 1. The significance of any non-zero value of r_s is then tested by

$$t = r_s \sqrt{\frac{N - 2}{1 - r_s^2}}. \quad (6.3)$$

t is well approximated by the *Student's distribution*².

The analysis gives coefficients of $r_s = 0.17$ for the full set of lines and $r_s = 0.08$ for the subset of 32 lines (see Figure 6.4). The latter being not significant at the 0.1% level (i.e., in only 0.1% of all cases a non-zero correlation can be deduced from a correlation coefficient of 0.08) thus in full agreement with no correlation. The obtained Spearman rank-order correlation coefficients occur in case of zero-correlation with probabilities of $\approx 1/3$ and $2/3$, respectively.

²Student's distributions are used instead of normal gaussian distributions when the population standard deviation is unknown and has to be estimated from the data. For large degrees of freedom it approaches the normal distribution.

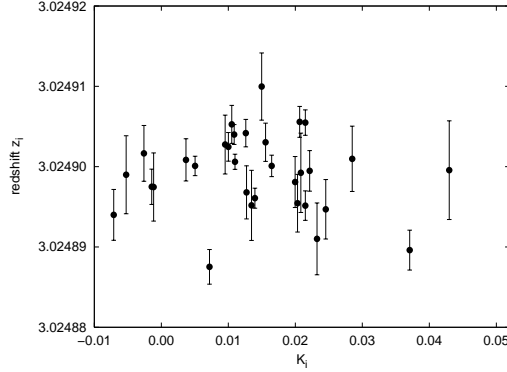


Figure 6.4: $z_i - K_i$ relation with individual redshifts for the reduced dataset of 32 lines in all observed rotational levels. With a Spearman rank-order correlation coefficient of $r_s = 0.08$ the data is in distinct agreement with no correlation.

assumed σ_{K_i}	$\Delta\mu/\mu$	z_{abs}
0	$(2.78 \pm 0.64) \times 10^{-5}$	3.024899
0.001	$(2.88 \pm 0.65) \times 10^{-5}$	3.024899

Table 6.2: Fits to the whole dataset with and without errors in K_i .

6.2.3 Fit to data with errors in both coordinates

A linear regression to fit a straight-line model $y(x) = a + b \times x$, or more specific $z_i = z_{\text{abs}} + b \times K_i$, can easily be achieved neglecting the errors in one of the variables. However, with respect to the low number of data points a fit to the data with errors in both coordinates seems to be more appropriate. The χ^2 merit function for this case is:

$$\chi^2(z_{\text{abs}}, b) = \sum_{i=1}^N \frac{(z_i - z_{\text{abs}} - b \times K_i)^2}{\sigma_{z_i}^2 + b^2 \times \sigma_{K_i}^2}. \quad (6.4)$$

According to Equation 2.28, the variation $\Delta\mu/\mu$ can be determined by $\Delta\mu/\mu = b/(1 + z_{\text{abs}})$ then. The procedure of such a fit is not trivial and was implemented from numerical recipes.

Studies of μ -variation so far have neglected the uncertainties of K_i as they seemingly have a much smaller influence on the regression than the errors in z_i . Table 6.2 lists the comparison of the two methods. Assuming an constant error for the K_i of 0.001 as stated in Reinhold et al. (2006), the changes in the results are indeed negligible. The most recent study argues further that the observational errors are hard to estimate and thus an unweighted fit would be more appropriate. Following that argument a $\Delta\mu/\mu$ of $(2.0 \pm 0.6) \times 10^{-5}$ is achieved in that

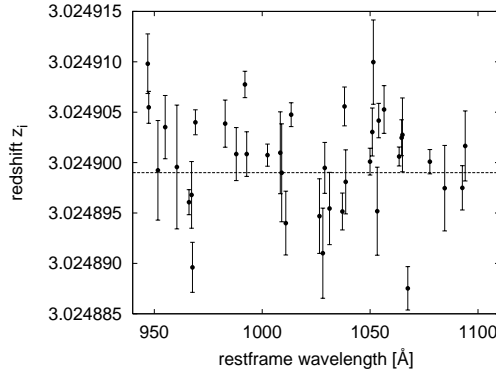


Figure 6.5: Measured redshifts in relation to the restframe wavelength to reveal a possible dependence. The dashed line represents z_{abs} .

work. A goodness of fit analysis can determine at what level the observational errors have an impact on the measured μ variation.

6.2.4 Goodness of fit

Goodness of fit means how well a statistical model fits a set of observations in contrast to a general σ of a fit which only states the confidence of the fit. The last section demonstrated the stability of a fit against a constant small error in the sensitivity coefficients. The χ^2 based fit (as described in Section 3.4.1) allows for a statement on the quality or rather the likelihood of a fit in respect to the model. The great advantage of the method used in this thesis to measure a possible μ variation is the simple model. The relation between measured redshift and computed sensitivity coefficient is stringently linear in case of variation. In case of no variation the gradient would be zero but still fit the assumed linear model. Figure 6.5 demonstrates that there is no detectable correlation between redshift and wavelength. Such a correlation would point out miscalibration of the spectra or major errors in the laboratory wavelengths. As a consequence, any result must be consistent with a linear correlation between z_i and K_i independently of a possible variation. The performed simulations of linefits indicated that the fit error on the observed wavelength for each line and thus the error in the relative redshift as estimated by the fitting programme are reasonable. This, of course, depends also on the accuracy of the errors given in the observed data. The correctness of the errors in the spectral data can be crudely tested by the χ^2 value of a reasonably good fit. However, the χ^2 is influenced by the trueness of the error as well as the accuracy of the model. A throughout value of χ^2 of ≈ 1 for the fitted lines with clean continuum sufficiently indicates a proper error given for the observed data. The mean value of all 351 fitted lines (39 lines in 9

scaling of σ_{z_i}	$\Delta\mu/\mu$	likelihood
1.0	$(2.88 \pm 0.65) \times 10^{-5}$	< 0.001
2.0	$(2.80 \pm 1.28) \times 10^{-5}$	0.23
2.2	$(2.80 \pm 1.40) \times 10^{-5}$	0.54

Table 6.3: Fits to the whole dataset of 39 lines with scaled errors in z_i .

spectra) is $\bar{\chi}^2 = 1.16$ with a more descriptive median³ of exactly 1.00. The mean χ^2 is expected to lie above the median due to the fact that for some absorption features the model of a single component is knowingly wrong and thus the flux is not fitted by the model for the whole evaluated range.

The goodness of fit for the fitted linear relation as in Table 6.2 gives a likelihood of the fit of $\ll 0.1\%$. Applying this goodness of fit analysis to the recently published data subset on Q0347-383 by Reinhold et al. (2006) gave a similar low result. This strongly indicates that the errors in general are underestimated. This conclusion is only valid when the model that was assumed holds true. A lowered likelihood can also emerge from measurement errors that are strongly non-normally distributed. The simulations with synthesised data, however, did show that the errors of the fit are in good agreement with a normal distribution for the lines selected. The validity of the assumed model is convincing and the errors of the fitted redshifts appear to be systematically underestimated. The fitted linear relation is not at all consistent with the observed data and the adopted error simply reflects the statistically best solution without considering consistency with the data. However, the likelihood of the fit scales rather strongly with the errors of the observed redshift. Assuming the greatest uncertainty in the measured redshifts despite the seemingly accurate output of the fitting program, the errors given for the redshifts were scaled by a constant factor. A scaling by factor two results in a likelihood of the fitted data of about 25% which would be acceptable, though still low.

This adaption of the error to be consistent with the stringent model, yields different results for the quality of the linear fit as shown in Table 6.3. The results in the table are based on all 39 observed lines still including the seven dubious lines that were discussed above.

³The mean value of a data set can be shifted by single values that have rather large scatter. A more robust expression is the *median* of a dataset. It describes a value for which larger and smaller values are equally probable. The *median* of a set of N elements x_i can be computed by sorting the dataset into ascending order and then evaluating: $x_{\text{med}} = x_{(N+1)/2}$, for odd N and $\frac{1}{2}(x_{(N/2)} + x_{(N/2+1)})$, for even N . The median is thus not affected by the scatter of single points.

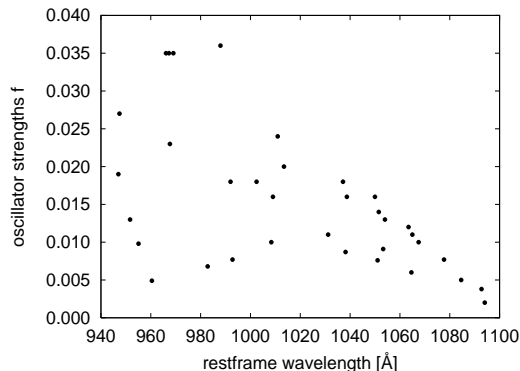


Figure 6.6: Oscillator strengths as computed by Abgrall and Herve in relation the restframe wavelength of the observed transitions. Note the spread towards higher energies.

6.3 Conclusions

Asking for self consistency in the result, brings down the significance of the measurement of a possible variation to $\approx 1\sigma$ at once. Rejecting the subset of seven lines of a single rotational level from the dataset leads to no correlation at all, since the correlation is already very weak as discussed above. A linear fit is no longer reasonable. A detection of a positive variation of μ forms solely from transitions for which $J = 1$ and $v > 7$ in the upper state, a range of transitions with significant non-BOA effects as reflected in the large changes in recently calculated K_i or λ_i for these vibrational bands. The discrepancy of the observed redshifts and their errors with the basic model of $\lambda_{\text{obs}} = \lambda_0 \times (z_{\text{abs}} + 1)$ hints towards yet not fully understood systematic errors. Possible reasons for the scatter in the redshift of several σ can be that a resolution of 53000 is not sufficient for precise linefits of unresolved H_2 features and thus the positioning error is systematically underestimated. Figure 6.6 shows the oscillator strengths for the observed H_2 lines which vary stronger for higher energies. The accuracy of the oscillator strengths cannot be easily verified and has a minor influence on the line position of a fit. However, the oscillator strengths of a line feature control the distinctiveness of the line shape and thus affect the certainty of a fit. This is especially the case at rather low signal to noise ratios.

A possible cause for differences in measured redshifts between the excitation levels can also be a spatially separation between the points of origin. The nature of DLAs is not yet fully understood and subject to several inconsistencies. Damped $\text{Ly}\alpha$ systems exhibit measured velocity widths of up to several hundred km s^{-1} and a median of about 90 km s^{-1} . This observed range is overall consistent with a rotating disc with velocities comparable to nearby galaxies. In fact this is in-

consistent with models of galaxies in the early universe. A mere differential of velocity towards the line of sight of a few hundred m/s corresponds to changes in redshift of $1 \times 10^{-6} - 1 \times 10^{-5}$, and thus in the dimension of the measured distribution. However, a scenario of a unidirectionalexited region of molecular hydrogen is unlikely. Spatially inhomogeneous excitation or abundance of molecular hydrogen in the DLA might still have a noticeable effect on the measured redshifts though it cannot explain the observed scatter.

Bandiera and Corbelli (2005) investigated a possible impact of gravitational redshift on the results of $\Delta\alpha/\alpha$ measurements. They report influences by gravitational redshifts on a scale to potentially mimic a variation. However, this effect solely appears in the case of misidentification of individual components, i.e., components were attributed to the same cloud in different transitions that are instead associated with different absorption systems. In the case of H_2 this seems rather unlikely and cannot explain the measured deviations in the redshift of the upper vibrational levels.

A possible variation of the proton-to-electron mass ratio cannot be confirmed. Furthermore the inconsistency of the data and the errors with respect to the scattering of the observed redshifts give reason to be more careful in formulating constraints as well. The resulting constraint at the 95% level is $|\Delta\mu/\mu| \leq 4.9 \times 10^{-5}$ over the period of ≈ 11.5 Gyr, or a decrease of $4.3 \times 10^{-15} \text{ yr}^{-1}$ for the hypothetical case of linear variation in time. The *light travel time* of 11.496 Gyr for $z = 3.025$ corresponds to the cosmological parameters $H_0 = 71 \text{ km s}^{-1}\text{Mpc}^{-1}$, $\Omega_M = 0.27$, $\Omega_{\text{vac}} = 0.73$.

7 Outlook

The method of measuring a possible variation of the proton-to-electron mass ratio appears to be quite straight forward and the model behind it is well defined. The remaining uncertainties emerge mainly from problems during the determination of the individual redshifts. The accuracy of the atomic data needs verification as well though their impact on the results may be small. The analysis of a possible variation via quasar spectroscopy using molecular hydrogen would gain by a multitude of different enhancements. On the methodical side further simulations are required to estimate the principal significance of results that can be expected from the data available would probably be most promising in the near future. These simulations could test how reproducible a positive detection of variation can be. For example applying a certain $\Delta\mu/\mu$ to a set of laboratory wavelength and perform a statistically informative number of simulated fits on a complete synthesised spectrum based on these modified restframe wavelengths and test the outcome for consistency with the input.

A significant positive result cannot be verified by the analysis in this work. In the near future laboratory experiments of extraordinary precision are expected by the use of frequency comb lasers. For this new principle the 2005 Nobel Prize was awarded to John Hall and Ted Hansch. A team at the Laser Centre Vrije Universite (LCVU) is currently involved in a project that among other things, aims for $\Delta\mu/\mu$ measurements that may already reach the disputed precision.

New data of DLAs with H₂ absorption features could be used to better determine different effects and systematic errors. In general a higher resolution is desirable to achieve a larger degree of confidence of the fitted parameters, mainly the broadening parameter. A better knowledge of the line shapes and more possible blends with lines that are possibly too weak to be tracked down via curve of growth analysis would increase the accuracy of the fitted line positions.

As the comparison of the nice separate spectra in section 3.2.2 illustrates, the scatter in derived positions decreases significantly with higher signal-to-noise ratios. The need for data with high S/N-ratios and high resolution for the task of detection of possible μ variation is abundantly clear. High precision in the reduction of the data is essential and probably a worthwhile subject for further studies.

The majority of theories behind variations of fundamental constants is yet non-specific. Possible variations of the fine structure constant $\Delta\alpha/\alpha$ and $\Delta\mu/\mu$ cannot be pulled together and must be observed independently. A variation of the or-

der of $2 \times 10^{-15} \text{yr}^{-1}$ is in the range of modern experiments in quantum optics. However, the results obtained under local conditions of laboratory experiments cannot be simply adopted to the universe even in case of a linear behaviour of variations in time. The so far conducted experiments are not directly aimed at $\Delta\mu/\mu$ measurements, since the methods require either the proton or electron mass to remain constant. Calmet and Fritzsche (2006) investigated possible scenarios of a change in proton mass without a variation of the electron mass, thus making $\Delta\alpha/\alpha$ and $\Delta\mu/\mu$ independent from each other. Barrow (2005) points out that the local observations are based on a gross cosmological overdensity on the order of 10^{30} times denser than the mean density of the background universe and therefore cannot substitute observations on cosmological scales. Other constraints are gained from linearly extrapolating possible variations in for example proton mass towards the big bang nucleosynthesis. Among the most popular scenarios of decreasing asymptotic change in nuclear masses some neglect the drastic influence this would have on timescales close to the recombination phase (Barshay and Kreyerhoff 2006). A theory formulated by Barrow and Magueijo (2005) predicts $\Delta\mu/\mu \leq 10^{-9}$ in case of mere change in proton mass and thus expects a strong correlation between $\Delta\mu/\mu$ and $\Delta\alpha/\alpha$ via the electron mass.

It is evident that further observational results and constraints are required. The application of quasar absorption spectroscopy appears to be the most promising approach. A direct increase of precision is to be expected from further state-of-the-art observational data.

Acknowledgements

I want to express my gratitude towards Prof. Dieter Reimers for giving me the unique opportunity to work in this absorbing field.

Also I am indebted to Dr. Robert Baade for the careful inspection of this work and numerous discussions on life, the universe, and everything. Thanks for raising the bar. I wish to specially thank my parents for their everlasting support that I took as a powerful back up. I also gained a lot by Dr. Cora Fechner's passed on enthusiasm that challenged even mine.

Special thanks also go to Diane for her kind understanding and herself.

"Not chaos-like, together crush'd and bruis'd,
But, as the world, harmoniously confused
Where order in variety we see,
And where, tho' all things differ, all agree."
-Pope, Windsor Forest

References

- H. Abgrall and E. Roueff. Wavelengths, oscillator strengths and transition probabilities of the H₂ molecule for Lyman and Werner systems. *A&AS*, 79:313–328, September 1989.
- H. Abgrall, E. Roueff, F. Launay, J. Y. Roncin, and J. L. Subtil. Table of the Lyman Band System of Molecular Hydrogen. *A&AS*, 101:273–+, October 1993.
- A.C. Aitken. On least squares and linear combinations of observations. *Proc.Roy.Soc.Edinburgh*, 55:42–48, 1934.
- R. Bandiera and E. Corbelli. Can hidden correlations mimic a variable fine structure constant? *A&A*, 434:543–552, May 2005.
- C.N. Banwell. *Fundamentals of Molecular Spectroscopy*. McGraw-Hill Publishing Company Limited, 1966.
- J. Barrow. Varying constants. *Royal Society of London Philosophical Transactions Series A*, 363:2139–2153, September 2005.
- J. D. Barrow and J. Magueijo. Cosmological constraints on a dynamical electron mass. *PhysRev*, 72(4):043521–+, August 2005.
- S. Barshay and G. Kreyerhoff. An asymptotic decrease of (m_p/m_e) with cosmological time, from a decreasing, small effective vacuum expectation value moving from a potential maximum in the early universe. *ArXiv Astrophysics e-prints*, June 2006.
- D. F. Buscher, J. T. Armstrong, C. A. Hummel, A. Quirrenbach, D. Mozurkewich, K. J. Johnston, C. S. Denison, M. M. Colavita, and M. Shao. Interferometric seeing measurements on Mt. Wilson: power spectra and outer scales. *Applied Optics*, 34:1081–+, February 1995.
- X. Calmet and H. Fritzsch. A Time Variation of Proton-Electron Mass Ratio and Grand Unification. *ArXiv Astrophysics e-prints*, May 2006.
- G. R. Carruthers. Rocket Observation of Interstellar Molecular Hydrogen. *ApJL*, 161:L81+, August 1970.

- H. Chand, R. Srianand, P. Petitjean, B. Aracil, R. Quast, and D. Reimers. Variation of the fine-structure constant: very high resolution spectrum of QSO HE 0515-4414. *A&A*, 451:45–56, May 2006.
- W. Demtröder. *Experimentalphysik 3*. Springer-Verlag Berlin Heidelberg New York, 2. Aufl., 2000.
- J. L. Dunham. The Energy Levels of a Rotating Vibrator. *Physical Review*, 41: 721–731, September 1932.
- G. Gamow. Electricity, Gravity, and Cosmology. *Physical Review Letters*, 19: 759–761, September 1967.
- Nikolaus Hansen and Andreas Ostermeier. Completely derandomized self-adaptation in evolution strategies. *Evolutionary Computation*, 9:159–195, 2001.
- G Herzberg. *Molecular Spectra and Molecular Structure*. New York: Van Nostrand, 1950.
- U. Hollenstein, E. Reinhold, C. A. de Lange, and W. Ubachs. LETTER TO THE EDITOR: High-resolution VUV-laser spectroscopic study of the Lyman bands in H₂ and HD. *Journal of Physics B Atomic Molecular Physics*, 39:L195–L201, April 2006.
- A. Ivanchik, P. Petitjean, D. Varshalovich, B. Aracil, R. Srianand, H. Chand, C. Ledoux, and P. Boissé. A new constraint on the time dependence of the proton-to-electron mass ratio. Analysis of the Q 0347-383 and Q 0405-443 spectra. *A&A*, 440:45–52, September 2005.
- D. E. Jennings, S. L. Bragg, and J. W. Brault. The V = 0 - 0 spectrum of H₂. *ApJL*, 282:L85–L88, July 1984.
- S. A. Levshakov, M. Dessauges-Zavadsky, S. D’Odorico, and P. Molaro. Molecular Hydrogen, Deuterium, and Metal Abundances in the Damped Ly α System at $z_{\text{abs}}=3.025$. *APJ*, 565:696–719, February 2002.
- S. A. Levshakov, M. Centurión, P. Molaro, S. D’Odorico, D. Reimers, R. Quast, and M. Pollmann. Most precise single redshift bound to $\Delta\alpha/\alpha$. *A&A*, 449: 879–889, April 2006.
- T. Lyman. Preliminary Measurement of the Short Wave-Lengths Discovered by Schumann. *ApJ*, 19:263–+, May 1904.
- D. Maoz, J. N. Bahcall, D. P. Schneider, N. A. Bahcall, S. Djorgovski, R. Doxsey, A. Gould, S. Kirhakos, G. Meylan, and B. Yanny. The Hubble Space Telescope Snapshot Survey. IV - A summary of the search for gravitationally lensed quasars. *ApJ*, 409:28–41, May 1993.

- P. J. Mohr and B. N. Taylor. CODATA recommended values of the fundamental physical constants: 2002. *Reviews of Modern Physics*, 77:1–107, March 2005.
- M. T. Murphy, J. K. Webb, V. V. Flambaum, C. W. Churchill, and J. X. Prochaska. Possible evidence for a variable fine-structure constant from QSO absorption lines: systematic errors. *MNRAS*, 327:1223–1236, November 2001.
- P. S. Osmer and M. G. Smith. Discovery and spectrophotometry of the quasars in the -40 deg zone of the CTIO Curtis Schmidt survey. *ApJS*, 42:333–349, February 1980.
- P. Petitjean, R. Srianand, and C. Ledoux. Molecular hydrogen at $z_{abs} = 1.973$ toward Q0013-004: dust depletion pattern in damped Lyman α systems. *MNRAS*, 332:383–391, May 2002.
- J Philip, J.P. Sprengers, Th. Pielage, C.A. Lange, W. Ubachs, and E Reinhold. highly accurate transition frequencies in the H₂ Lyman and Werner absorption bands. *Can. J. Chem*, 82:712–722, 2004.
- W. H. Press, S. A. Teukolsky, W. T. Vetterling, and B. P. Flannery. *Numerical recipes in C. The art of scientific computing*. Cambridge: University Press, —c1992, 2nd ed., 1992.
- R. Quast, R. Baade, and D. Reimers. Evolution strategies applied to the problem of line profile decomposition in QSO spectra. *A&A*, 431:1167–1175, March 2005.
- E. Reinhold, R. Buning, U. Hollenstein, A. Ivanchik, P. Petitjean, and W. Ubachs. Indication of a Cosmological Variation of the Proton-Electron Mass Ratio Based on Laboratory Measurement and Reanalysis of H₂ Spectra. *Physical Review Letters*, 96(15):151101–+, April 2006.
- B. D. Savage, R. C. Bohlin, J. F. Drake, and W. Budich. A survey of interstellar molecular hydrogen. I. *ApJ*, 216:291–307, August 1977.
- D. A. Varshalovich and S. A. Levshakov. On a time dependence of physical constants. *Journal of Experimental and Theoretical Physics Letters*, 58:237–240, August 1993.
- D. A. Varshalovich and A. Y. Potekhin. Cosmological Variability of Fundamental Physical Constants. *Space Science Reviews*, 74:259–268, November 1995.
- J. K. Webb, M. T. Murphy, and V. V. Flambaum. Do Constants Change? *The Astrochemistry of External Galaxies, 25th meeting of the IAU, Joint Discussion 21, 23 July 2003, Sydney, Australia*, 21, 2003.

- A. Wolfe, E. Gawiser, and J. Prochaska. Damped Ly α Systems. *Annu.Rev.Astron.Atrophys.*, 43:861–918, 2005.
- A. M. Wolfe, K. M. Lanzetta, C. B. Foltz, and F. H. Chaffee. The Large Bright QSO Survey for Damped LY alpha Absorption Systems. *ApJ*, 454:698–+, December 1995.

Erklärung

Hiermit versichere ich, dass ich die vorliegende Arbeit selbständig und nur unter Verwendung der angegebenen Quellen und Hilfsmittel angefertigt habe. Nach der Begutachtung verbleibt ein Exemplar der vorliegenden Arbeit in der Bibliothek. Mit der zukünftigen Ausleihe der Diplomarbeit erkläre ich mich einverstanden.

Hamburg, 19th September 2006

Martin Wendt